

1 This manuscript is a *preprint* and has been accepted for publication in  
2 *Precambrian Research*. Please cite as:

3  
4 Barreto, C.J.S., Haag, M.B., Lafon, J.M., Sommer, C.A., da Rosa-Costa,  
5 L.T., 2021. Textural analysis and emplacement conditions of well-  
6 preserved Orosirian felsic volcanic rocks of northern Amazon Craton,  
7 Brazil. *Precambrian Research* 366, 106437.

8 <https://doi.org/10.1016/j.precamres.2021.106437>  
9

10

11

12

13

14

15

16

17

18

19

20

21

22

23

24

25

26

27

28

## Textural analysis and emplacement conditions of well-preserved Orosirian felsic volcanic rocks of Northern Amazon Craton, Brazil

Carla Joana Santos Barreto<sup>a\*</sup>, Mauricio Barcelos Haag<sup>b,c</sup>, Jean Michel Lafon<sup>d</sup>, Carlos Augusto Sommer<sup>b</sup>, Lúcia Travassos da Rosa-Costa<sup>e</sup>

<sup>a</sup> Departamento de Geologia, Universidade Federal de Pernambuco. Av. Arquitetura s/n, Recife-PE, Brazil.

<sup>b</sup> Instituto de Geociências, Universidade Federal do Rio Grande do Sul. Av. Bento Gonçalves 9500, Rio Grande do Sul-RS, Brazil.

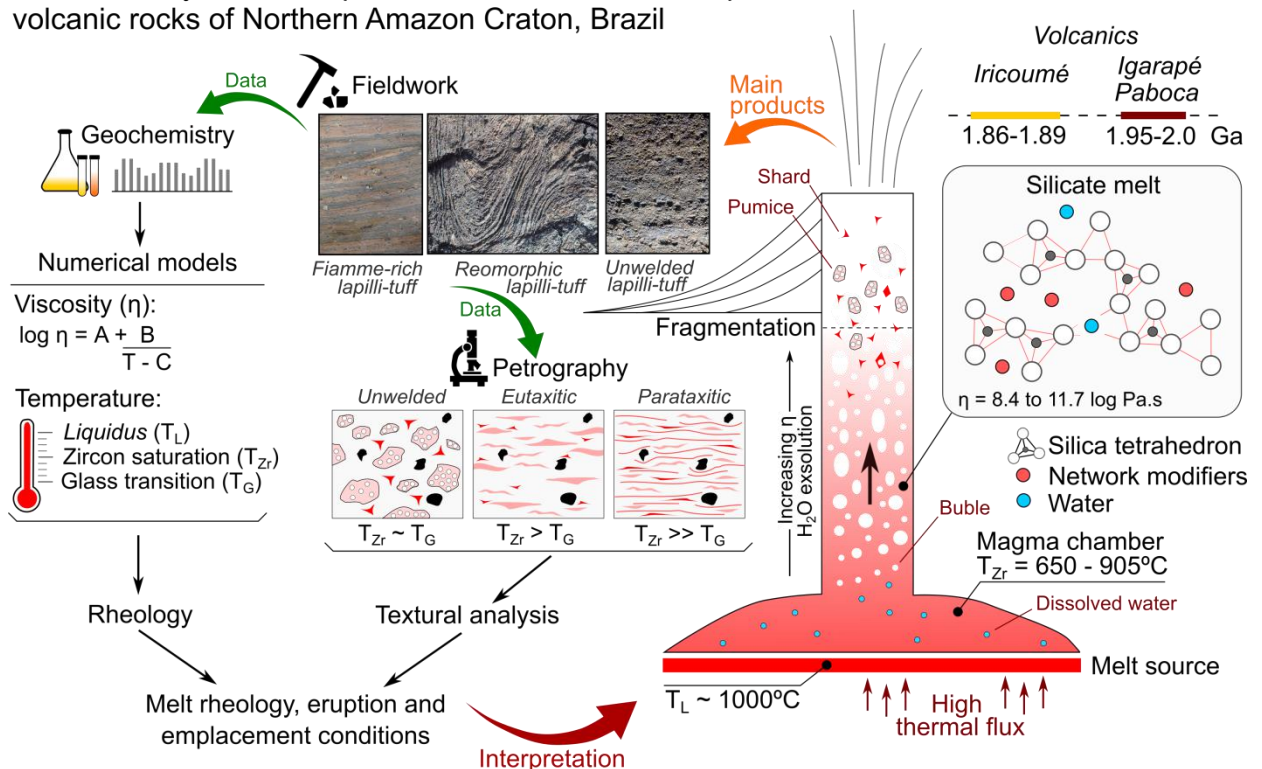
<sup>c</sup> Department of Earth Sciences, University of Toronto. 22 Ursula Franklin Street, Toronto, ON, M5S 3B1, Canada.

<sup>d</sup> Instituto de Geociências, Universidade Federal do Pará. Rua Augusto Corrêa 1, Belém-PA, Brazil.

<sup>e</sup> Serviço Geológico do Brasil, Companhia de Pesquisa de Recursos Minerais, Av. Perimetral 3645, Belém-PA, Brazil.

\* corresponding author: [carla.barreto@ufpe.br](mailto:carla.barreto@ufpe.br)

### Textural analysis and emplacement conditions of well-preserved Orosirian felsic volcanic rocks of Northern Amazon Craton, Brazil



51 **Abstract**

52 Located in the Amazon Craton, the Uatumã magmatism (1.89-1.87 Ga) consists in one  
53 of the oldest Silicic Large Igneous Provinces (SLIPs) on Earth. For a long time, the access  
54 to these deposits in the northern Amazon Craton (Erepecuru–Trombetas Domain) has been  
55 set back for volcanological studies due to dense vegetation cover and the absence of roads.  
56 Recent studies identify two Orosirian volcanic units in the region: the Iricoumé Group  
57 (1.89-1.87 Ga) related to the Uatumã magmatism, and the Igarapé Paboca Formation (1.99-  
58 1.94 Ga), associated to an older magmatism. Both units are widespread in the Erepecuru–  
59 Trombetas Domain and include effusive and explosive deposits. In this paper, we apply  
60 textural analyses and rheological estimations to determine the eruption and emplacement  
61 conditions of these two volcanic sequences. Textural analyses were carried out through  
62 fieldwork and petrography, including a systematic classification of lavas and volcanoclastic  
63 rocks. Rheological parameters were determined using geochemistry data to obtain melt  
64 viscosity ( $\eta$ ) and temperature, zircon saturation ( $T_{Zr}$ ), liquidus ( $T_L$ ), and glass transition  
65 temperatures ( $T_G$ ), for anhydrous and hydrous compositions. Textural analyses indicate the  
66 predominance of volcanoclastic facies with abundant eutaxitic and parataxitic textures.  
67 Rheological estimations reveal  $T_L$  of 1020°C,  $T_{Zr}$  650-905°C, and  $T_G$  640-753°C for  
68 anhydrous Iricoumé Group melts. Eruptive viscosity estimations range from 8.4 to 11.7 log  
69  $\eta$  (Pa.s). Igarapé Paboca melts present higher temperatures, with  $T_L$  of 1050°C,  $T_{Zr}$  710-  
70 880°C, and  $T_G$  670-740 °C. Modeling using hydrous compositions indicate that minute  
71 amounts of water can strongly affect the rheology of the studied melts, reducing  $\eta$ ,  $T_L$ ,  $T_{Zr}$ ,  
72 and  $T_G$ . The petrographic features indicative of hydrous magma reinforces the role of H<sub>2</sub>O  
73 as a controlling agent in the fragmentation of Iricoumé and Igarapé Paboca melts. The  
74 pyroclastic samples are marked by elevated  $\Delta T_{Zr} - T_G$  relationships indicative of high  
75 emplacement temperatures above the  $T_G$ . Our results indicate that the high temperatures  
76 and the presence of network-modifier cations in the studied melts favored the development  
77 of extensive welded ignimbrites associated with low-eruption columns, likely developed in  
78 fissural and/or caldera systems.

79

80 **Keywords:** Orosirian volcanism; Felsic ignimbrite; Magma rheology; Amazon craton;  
81 Welding; Silicic Large Igneous Province.

## 82 **1. Introduction**

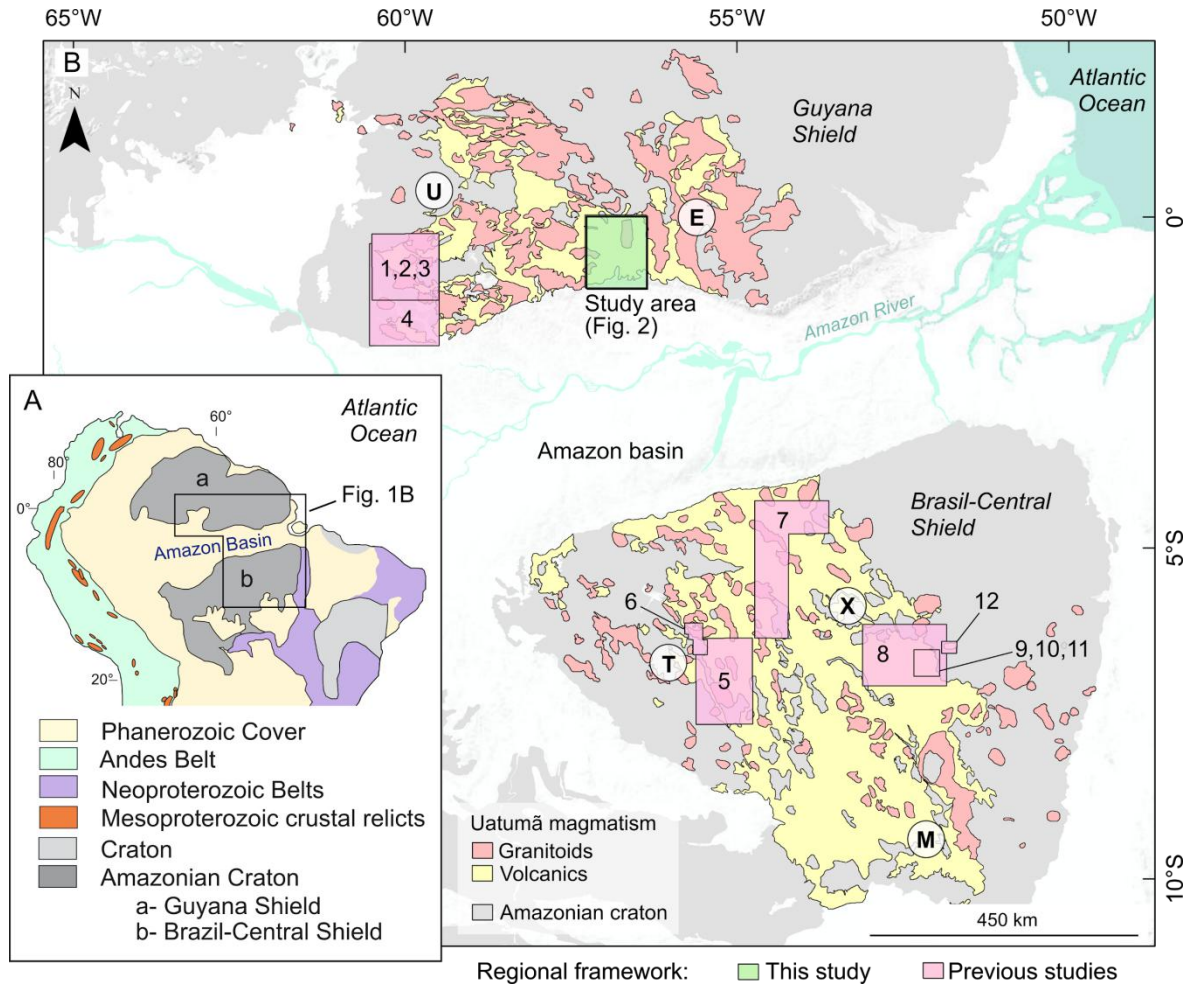
83 Located in the northeastern section of South America (Fig. 1A), the Amazonian  
84 Craton consists of the largest Precambrian domain in the South American Platform  
85 (Almeida et al., 1981). This terrane hosts some of the most important mineral deposits of  
86 the world (e.g., Juliani et al., 2005; Bettencourt et al., 2016; Motta et al., 2019), as well as a  
87 significant geological record of the Paleoproterozoic period. The widespread Uatumã  
88 volcano–plutonic event (1.89–1.87 Ga) covers 1.2 million km<sup>2</sup> of the Amazonian Craton  
89 (Fig. 1B, Guiana and Brazil Central shields) and is considered by several authors a Silicic  
90 Large Igneous Province (SLIP; Teixeira et al., 2019 and references therein). This Orosirian  
91 magmatic province is considered one of the most intriguing magmatic events of the world,  
92 with abundant explosive, effusive and intrusive rocks that are still poorly constrained due  
93 to dense vegetation cover (Schobbenhaus and Brito Neves, 2003; Brito Neves, 2011;  
94 Fernandes et al., 2011; Juliani et al., 2011; Klein et al., 2012; Barreto et al., 2013, 2014;  
95 Roverato et al., 2019; Teixeira et al., 2019).

96 The Guiana Shield represents the northern portion of the Amazonian Craton, to the  
97 north of the Amazon Basin (Fig. 1B). This area has been subdivided into several tectonic-  
98 geochronological provinces (Santos et al., 2000, 2006; Tassinari and Macambira, 2004)  
99 and tectonic–stratigraphic domains based on geological, geochronological, structural and  
100 geophysical data (Reis et al., 2003, 2006; Vasquez and Rosa-Costa, 2008). Located in the  
101 Brazilian part of the central-south Guiana Shield, the Erepecuru–Trombetas Domain (Fig.  
102 1A) documents two Orosirian magmatic events separated by 100 Ma. These events include  
103 the Uatumã magmatism, which volcanic rocks have been grouped in the Iricoumé Group  
104 (1.89–1.87 Ga), and an older volcanism, related to Orocaima Event, grouped in the Igarapé  
105 Paboca Formation (1.99–1.94 Ga) (Castro et al., 2014; Silva et al., 2019). Both the  
106 Iricoumé Group and the Igarapé Paboca Formation consist of explosive and effusive

107 volcanic rocks of felsic to intermediate compositions with well-preserved textures and  
108 structures that record the dynamics of this volcanism.

109 For a long time, access to these units and the Erepecuru–Trombetas Domain was  
110 hampered for systematic geological and geochronological studies due to the scarcity of  
111 roads. As a result, studies on the Uatumã magmatism have been concentrated in Tapajós  
112 and Iriri-Xingu domains, in the Brazil Central Shield (Fig. 1B - e.g. Lamarão et al., 2002;  
113 Fernandes et al., 2006; Juliani and Fernandes, 2010; Fernandes et al., 2011; Semblano et al.,  
114 2016; Lagler et al., 2019; Roverato et al., 2019) and in the Pitinga mining district of the  
115 Uatumã-Anauá Domain (Fig. 1B - e.g. Ferron et al., 2010; Pierosan et al., 2011a, 2011b;  
116 Simões et al., 2014a). Recent geological mapping performed by the Geological Survey of  
117 Brazil (Castro et al. 2014; Silva et al., 2019) in addition to petrographical, geochemical,  
118 and geochronological studies (Barreto et al., 2013, 2014; Leal et al., 2015, 2018; Silva et al.  
119 2019) improved the geological knowledge of this domain. However, investigations of  
120 emplacement mechanisms and volcanic processes in the Erepecuru–Trombetas Domain are  
121 still scarce.

122 This study aims to improve the current knowledge about the volcanic rocks of the  
123 Iricoumé Group and the Igarapé Paboca Formation in the southern-central Guiana Shield.  
124 In order to achieve this purpose, we applied textural analysis to define coherent and  
125 volcanoclastic facies. For volcanoclastic samples, we also established a ranking of welding  
126 intensity. To explore the conditions of emplacement of the ancient Uatumã SLIP and older  
127 volcanics, we used geochemical data to obtain temperature and viscosity estimations using  
128 zircon saturation, liquidus, and glass transition temperatures. Based on textural features  
129 and the rheological parameters, we determine the eruption and emplacement mechanisms  
130 of the Iricoumé Group and Igarapé Paboca Formation to reconstruct part of the Orosirian  
131 volcanism.



132 **Fig. 1.** A) Map of South America highlighting the Amazonian Craton and its subdivision into the a)  
133 Guiana Shield and the b) Brazil-Central Shield (modified from Fraga and Cordani, 2019); B) Occurrence of  
134 the Uatumã magmatism in the Amazonian craton, identified in the study area and previously studied regions:  
135 1 - Ferron et al. (2010), 2 - Piosan et al. (2011a), 3 - Piosan et al. (2011b), 4 - Simões et al. (2014a), 5 -  
136 Roverato et al. (2019), 6 - Lamarão et al. (2002), 7 - Semblano et al. (2016), 8 - Roverato et al. (2019), 9 -  
137 Fernandes et al. (2006), 10 - Juliani and Fernandes (2010), 11 - Fernandes et al. (2011), 12 - Lagler et al.  
138 (2019). Tectonic Domains: U: Uatumã-Anauá; E: Erepecuru-Trombetas; T: Tapajós; X: Iriri-Xingu; M:  
139 North Mato Grosso. Based on Cordani et al. (2016).

140

## 141 2. Geological background

142 Located in the Amazon Craton, the Erepecuru–Trombetas Domain is constituted  
143 by Archean and/or Paleoproterozoic basement units (undifferentiated complex and  
144 volcano-sedimentary sequences), two Orosirian magmatic associations (ages ca. 2.0-1.95  
145 Ga and 1.89-1.86 Ga), and Paleoproterozoic and Paleozoic sedimentary rocks.

146 Undifferentiated mafic rocks, diabases, and nepheline syenites are also identified in the  
147 region (Vasquez and Rosa-Costa, 2008). The study area is located in the central-south  
148 segment of the Erepecuru–Trombetas Domain. In this area, two Orosirian magmatic  
149 associations are the dominant, whereas basement outcrops are absent. The available zircon  
150 U-Pb and Pb-Pb radiometric data on the Orosirian magmatic rocks of the Erepecuru-  
151 Trombetas domain are presented in Table 1.

Geological unit	Rock type	U-Pb zircon Age (Ma)	Pb-Pb zircon Age (Ma)	Ref.
<i>Old Orosirian magmatism</i>				
<b>Caxipacoré Suite</b>	Syenogranite		1977 ± 4	1
	Monzogranite		1982 ± 9	1
	Quartz-monzonite	1986 ± 5		2
	Monzogranite	1986 ± 4		2
	Monzogranite	1991 ± 6		3
	Monzogranite	1989 ± 7		3
	Monzogranite	1995 ± 19		4
<b>Igarapé Taboca Formation</b>	Andesite		1992 ± 3	5
	Andesitic ignimbrite	1948 ± 6		2
<i>Uatumã magmatism</i>				
<b>Água Branca Suite</b>	Monzonite	1887 ± 5		3
<b>Mapuera Suite</b>	Granite	1881 ± 8		3
	Granite		1889 ± 2	6
	Granite		1861 ± 20	6
<b>Iricoumé Group</b>	Andesite	1889 ± 9		2
	Trachydacitic Ignimbrite		1888 ± 3	5
	Trachydacitic Ignimbrite		1889 ± 2	5

152

153 **Table 1.** Zircon U-Pb and Pb-Pb radiometric data on the Orosirian magmatic rocks of the Erepecuru-  
154 Trombetas Domain. References: 1. Leal et al. (2015); 2. Silva et al. (2019); 3. Leal et al. (2018); 4. Vianna et  
155 al. (2017); 5. Barreto et al. (2013); 6. Castro et al. (2014).

156

157 The older magmatic association (2.0-1.95 Ga) is constituted by granites included in the  
158 Caxipacoré Suite and volcanic rocks (effusive and pyroclastic) of the Igarapé Paboca

159 Formation. The Caxipacoré Suite consists of alkali feldspar granites, syenogranites,  
160 monzogranites, and granodiorites, whereas the Igarapé Paboca Formation comprises  
161 andesites, dacites, and subordinate trachyandesites, trachytes, ignimbrites, tuffs, and  
162 breccias.

163 Both volcanic and plutonic rocks present a high-K to shoshonitic, calc-alkaline  
164 signature related to arc-setting (Barreto et al., 2014; Leal et al., 2018; Silva et al., 2019).  
165 The Caxipacoré granitoids show U-Pb and Pb-Pb zircon ages around 1.96-1.99 Ga (; Leal  
166 et al., 2015, 2018; Silva et al., 2019; Vianna et al., 2017), whereas the Igarapé Paboca  
167 Formation displays U-Pb and Pb-Pb zircon ages between 1.99 and 1.95 Ga (Barreto et al.,  
168 2013; Castro et al., 2014; Silva et al., 2019).

169 The younger volcano-plutonic association (1.89-1.86 Ga), related to the Uatumã event,  
170 is constituted by granitic rocks of Água Branca and Mapuera suites and the volcanic rocks  
171 of the Iricoumé Group. Both granitoid suites and the Iricoumé volcanics are considered  
172 coeval (Table 1 and Fig. 2). However, the Iricoumé Group and Mapuera Suite, (which  
173 predominate in the study area) share similar geochemical characteristics that are distinct  
174 from the Água Branca granitoids (Barreto et al., 2014; Leal et al., 2018; Silva et al., 2019).  
175 The granitoids of the Mapuera Suite comprise alkali feldspar granites, syenogranites, and  
176 monzogranites with A-type affinity. Pb-Pb and U-Pb zircon ages range between  $1889 \pm 2$   
177 and  $1861 \pm 20$ Ma (Castro et al., 2014; Leal et al., 2018; Silva et al., 2019).

178 The Iricoumé Group is composed of undeformed and unmetamorphosed effusive,  
179 pyroclastic, and subvolcanic volcanic rocks of felsic to intermediate composition with K-  
180 high calc-alkaline to shoshonitic signatures and A-type magma affinity. The available  
181 geochronological Pb-Pb and U-Pb zircon data for these rocks suggest a narrow range of  
182 volcanism ages, from 1.89-1.88 Ga (Barreto et al., 2013; Silva et al., 2019).

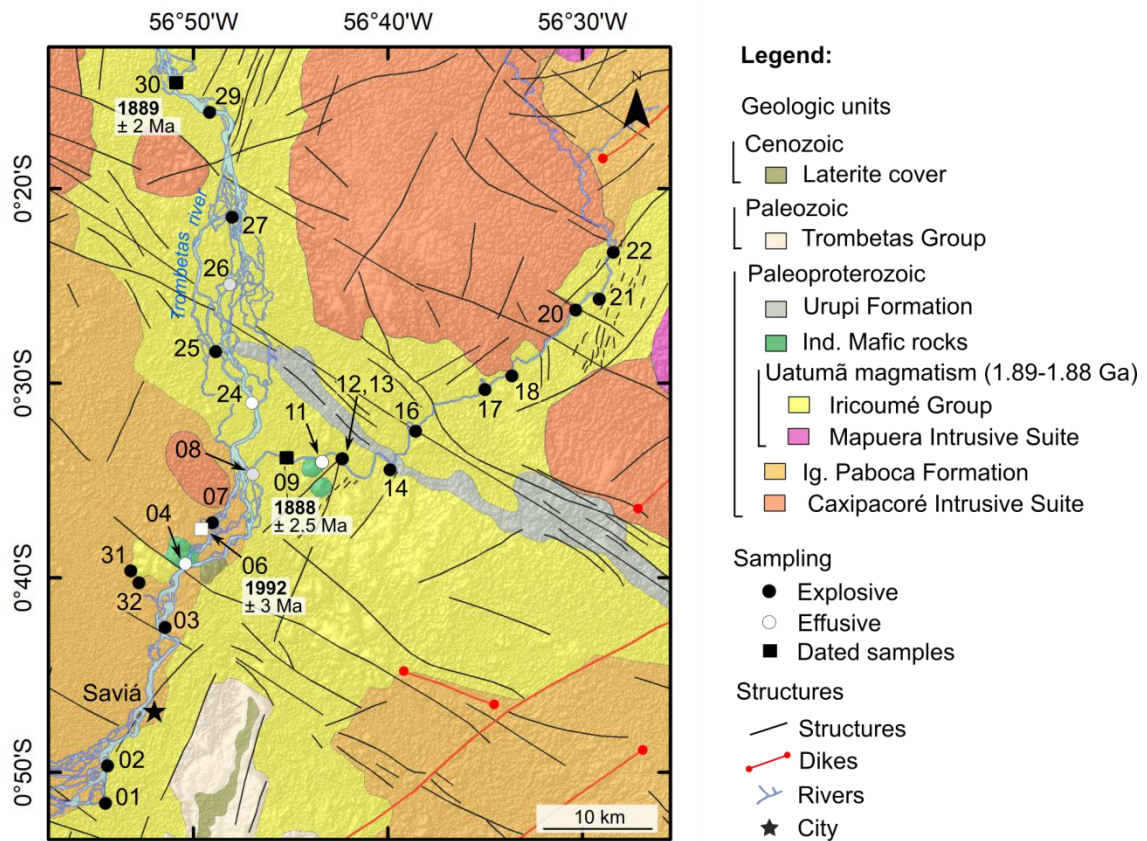


183 The 1.89-1.88 Ga Uatumã volcanism has been studied in detail in several domains of  
184 the Amazon Craton (e.g., Costi et al., 2000; Klein and Vasquez, 2000; Reis et al., 2000,  
185 2006; Lamarão et al., 2002, 2005; Almeida, 2006; Fernandes et al., 2006, 2011; Ferron et  
186 al., 2006, 2010; Valério et al., 2009; Pierosan et al., 2011a, 2011b; Klein et al., 2012;  
187 Barreto et al., 2013, 2014; Marques et al., 2014). The designation of Iricoumé Group is  
188 used for volcanic rocks outcropping in the Erepecuru-Trombetas and Uatumã-Anauá  
189 domains to the north of the Amazon Basin. To the south of this basin, correlated volcanic  
190 rocks occur in the Iriri-Xingu Domain under the designations of Sobreiro and Santa Rosa  
191 formations (Fernandes et al., 2006, 2011; Roverato, 2016; Roverato et al., 2017). In the  
192 Tapajós Domain, the correlated volcanic rocks are grouped in the Moraes Almeida  
193 Formation of the Iriri Group (Klein and Vasquez, 2000; Lamarão et al., 2002; Juliani et al.,  
194 2005).

195 Several undifferentiated small mafic rock bodies intrude rocks of the Iricoumé Group  
196 and Igarapé Paboca Formation. Geochronological data is still not available for these rocks,  
197 which has been interpreted by Vasquez and Costa (2008) as intra-plate mafic magmatism  
198 related to either Orosirian ( $\approx 1.88$  Ga) or Statherian ( $\approx 1.78$  Ga) crustal extension.

199 The Urupi Formation outcrops in the study area as an elongated ridge with NW–SE  
200 direction. This sedimentary formation includes sandstones, arkoses, and siltstones  
201 intercalated with volcanoclastic rocks (silicified tuffs and ignimbrites). The maximum age  
202 for this formation has been established at ca. 1.88-1.86 Ga based on the ages of the  
203 underlying Iricoumé volcanic rocks. Minimum age of 1.78 Ga was obtained with the U-Pb  
204 zircon dating of diabase sills, which are intrusive in the Urupi Formation (Santos et al.,  
205 2002). Recently, two groups of U-Pb LA-ICPMS ages of 2167-2050 Ma and 2761-2574  
206 Ma were obtained for detrital zircons of the Urupi Formation, (Magalhães et al., 2017).

207 The Trombetas Group is composed of sandstones, shales, and siltstones that  
208 correspond to the early stages of Paleozoic deposition of the Amazon Basin with  
209 transgressive-regressive characteristics. As field data are lacking, the available information  
210 about this unit was obtained from remote-sensing interpretations (Silva et al., 2019). The  
211 rocks of this group occur in the southern limit of the studied region and show a pronounced  
212 relief with well-fitted drainage and V-shaped valleys, which contrasts with the low-relief of  
213 the Precambrian units of the Igarapé Paboca Formation and the Iricoumé Group.



214 **Fig. 2.** Location map (see also Fig. 1B) with sampling sites and main geologic units. For a sample list of  
215 geological units, please check Table 2. Geochronological data from Barreto et al. (2013). Map modified from  
216 Silva et al. (2019), shaded relief derived from ALOS PALSAR digital elevation model  
217 (<https://vertex.daac.asf.alaska.edu/>).  
218  
219  
220  
221

222 **3. Methods**

223 *3.1 Petrography*

224 The fieldwork was performed by SBG-CPRM team during the project of mapping of  
225 the Pará state (Castro et al., 2014; Silva et al., 2019). For this study, the CPRM-Belém  
226 provided the outcrop photographs and samples. From the most representative samples, 18  
227 thin sections were prepared and described using a Leica DM4500 digital microscope model  
228 with an attached camera (LEICA DFC495 model).

229 *3.1.1 Ranking welding intensity*

230 To compare our volcanoclastic samples, we present a scheme for ranking welding  
231 intensity in pyroclastic rocks, which comprises five ranks (I-IV) defined according to  
232 macroscopic and microscopic textural characteristics. Our classification is based on the  
233 Quane and Russel (2004) scheme to characterize welding intensity, with some  
234 modifications in order to highlight the differences observed in the studied samples. Our  
235 scheme includes incipiently welded (rank I), moderately welded with eutaxitic texture  
236 (rank II), and strongly welded with parataxitic texture (rank III). The petrographic  
237 descriptions used to define each rank as well as the equivalences with the scheme from  
238 Quane and Russel (2004) are listed in Table 2. Field and petrography data are depicted in  
239 Figures 3 to 7 to illustrate the textural categories and the main characteristics of each rank.

240

241 *3.2 Whole-rock geochemistry*

242 The studies of textural analysis and imaging were performed in 18 samples of the  
243 Erepecuru-Trombetas Domain, including 3 hypabyssal rocks, 2 lavas, and 13 ignimbrites  
244 rich in juvenile fragments. The whole-rock chemical analyses of these samples were  
245 performed at ACME Laboratories Ltd (Vancouver, Canada). Major oxides were obtained  
246 by inductively coupled plasma atomic emission spectrometry (ICP-AES), while the Zr trace

247 element was analyzed by inductively coupled plasma atomic mass spectrometry (ICP-MS).  
248 The analytical protocol at the ACME laboratory included the analysis of standard STD SO-  
249 18 and BLK and of three sample duplicates (LT-03, LT-13, and LT-32). The representative  
250 geochemical results are presented in Table 2 and plotted in the  $\text{SiO}_2$  vs  $\text{Zr/TiO}_2$   
251 classification diagram (Fig. 8) using the GeoChemical Data toolkit v. 2.3 software  
252 (available at <http://www.gcdkit.org/gcdkit-publications/>).

253

### 254 *3.3 Rheology*

255 Based on geochemical data, we estimated rheological parameters for the ignimbrites  
256 and lavas of the Iricoumé Group and Igarapé Paboca Formation (Table 3) using the  
257 numerical models of Watson and Harrison (1983), Sisson and Groove (1993), and  
258 Giordano et al. (2008).

259 We applied the model of Watson (1979) and Watson and Harrison (1983) to estimate  
260 magma temperatures using the zircon saturation geothermometer ( $T_{\text{Zr}}$ ). The Zircon  
261 saturation method has been successfully applied to igneous and volcanic rocks, allowing  
262 the determination of transport and emplacement mechanisms (e.g., Liu et al., 2013). We  
263 used the model of Sisson and Groove (1993) to determine the liquidus temperature ( $T_{\text{L}}$ ),  
264 which represents the magma generation temperature and can give clues about the  
265 geotectonic and thermal regime of the region.

266 The model of Giordano et al. (2008) was applied to calculate the melt viscosity ( $\eta$ ) and  
267 the glass transition temperature ( $T_{\text{G}}$ ). While  $T_{\text{L}}$  indicates the maximum temperature,  $T_{\text{G}}$   
268 reflects the boundary temperature between a ductile (above  $T_{\text{G}}$ , allowing viscous flow,  
269 pyroclastic sintering, and welding) and a fragile (below  $T_{\text{G}}$ , allowing only elastic  
270 deformation) behavior of a silicate melt (Webb, 1997; Giordano et al., 2005). A detailed  
271 description of rheological calculations is given in Supplementary material A, B, C, and D.

272 All mentioned parameters were estimated using both anhydrous and wet compositions  
273 with 0.25, 1.0, 2.0, and 4.0 wt% of H<sub>2</sub>O, to evaluate the effect of dissolved magmatic water  
274 on the studied melts.

275

## 276 **4. Results**

### 277 *4.1. Field and faciological aspects*

278 Ignimbrites are the main volcanic deposits in the area and are characterized by  
279 eutaxitic and parataxitic textures (Fig. 3A-3C) with low to moderate inverse grading (Fig.  
280 3D). These rocks are generally moderately to poorly sorted, with fragment sizes ranging up  
281 to lapilli (Fig. 3E) of plagioclase, sanidine, and quartz crystals, as well as sub-angular to  
282 sub-rounded lithic clasts and pumices (Fig. 3F). The groundmass of these deposits  
283 generally includes pumices and fiammes (Fig. 3A, 3B, 3C, 3F) and sometimes fiammes  
284 with spherulitic texture (Fig. 3G). Subordinately, some samples of crystal-rich ignimbrites  
285 also occur in the studied area and are characterized by crystal contents of up to 40% (vol.),  
286 mainly composed of quartz and feldspar (Fig. 3H).

287 The rheomorphic ignimbrites show subhorizontal bands (Fig. 4A), boudinage fiamme  
288 characterizing the parataxitic texture, and sometimes tight isoclinal folds at the outcrop  
289 scale (Fig. 4B-4C). These rheomorphic ignimbrites show angular-shaped broken crystal  
290 fragments of plagioclase and lithic clasts with sizes ranging from ash to lapilli (Fig. 4D).  
291 Often these ignimbrites show all fiamme collapsed and the parataxitic texture is faintly  
292 visible, which could led to a false interpretation of porphyritic texture (Fig. 4D).

293 Minor occurrences of effusive deposits, including lava and subvolcanic rocks, have  
294 been described in close association with the explosive deposits. The lavas are crystal-rich  
295 andesitic and show massive structure as well as porphyritic texture, characterized by high  
296 concentration (more than 35% vol.) of plagioclase and amphibole phenocrysts (Fig. 4E).

297 The subvolcanic rocks comprise two groups of rocks: lamprophyres and dacites. The  
298 lamprophyres are massive and porphyritic, characterized by amphibole phenocrysts set in  
299 an aphanitic matrix (Fig. 4F). Dacitic rocks exhibit flow-foliations at outcrop scale (Fig.  
300 4G) and alkali feldspar and plagioclase porphyries set in an aphanitic groundmass at a  
301 macroscopic scale (Fig. 4H).

302

303

304

305

306

307

308

309

310

311

312

313

314

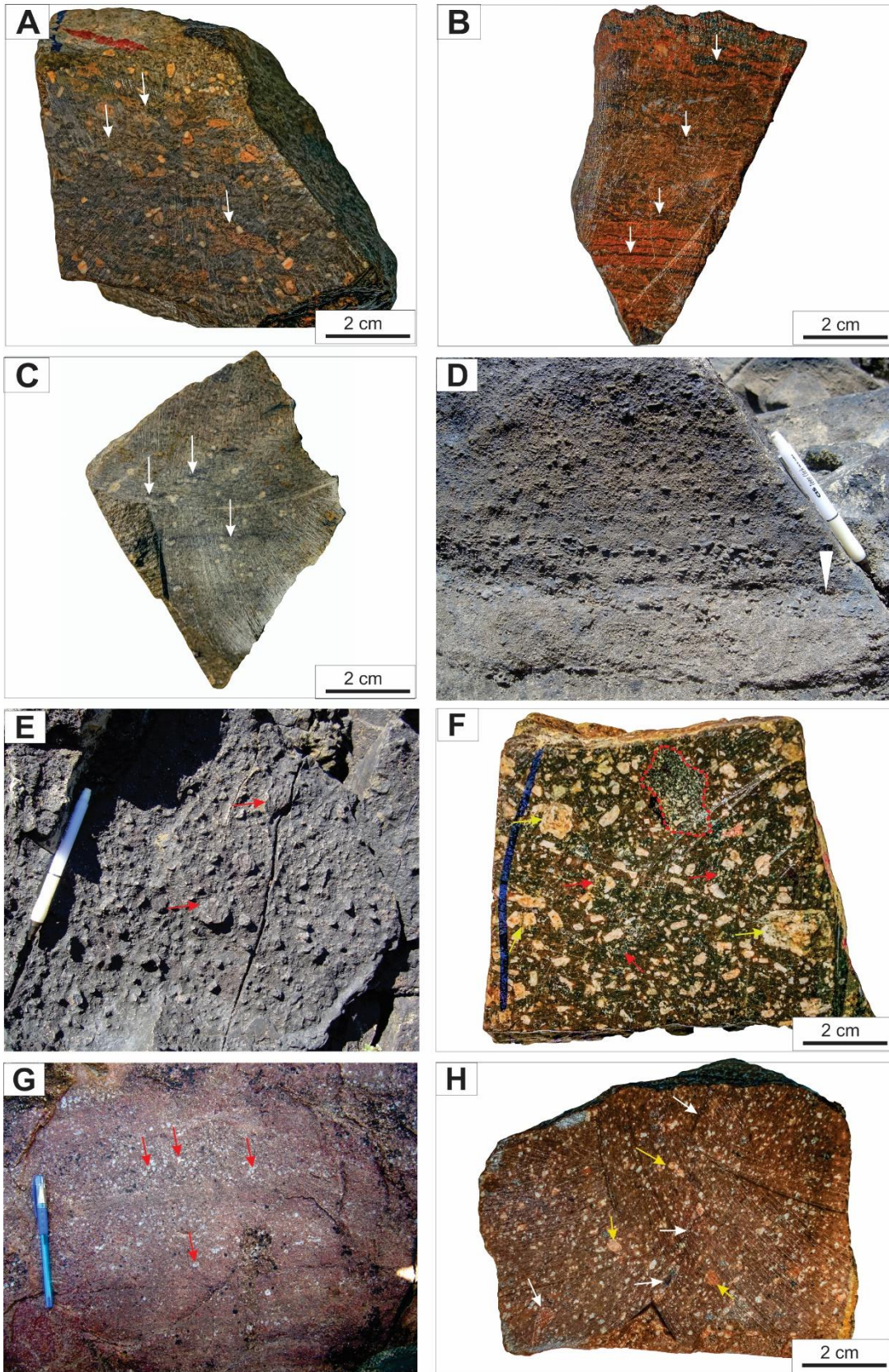
315

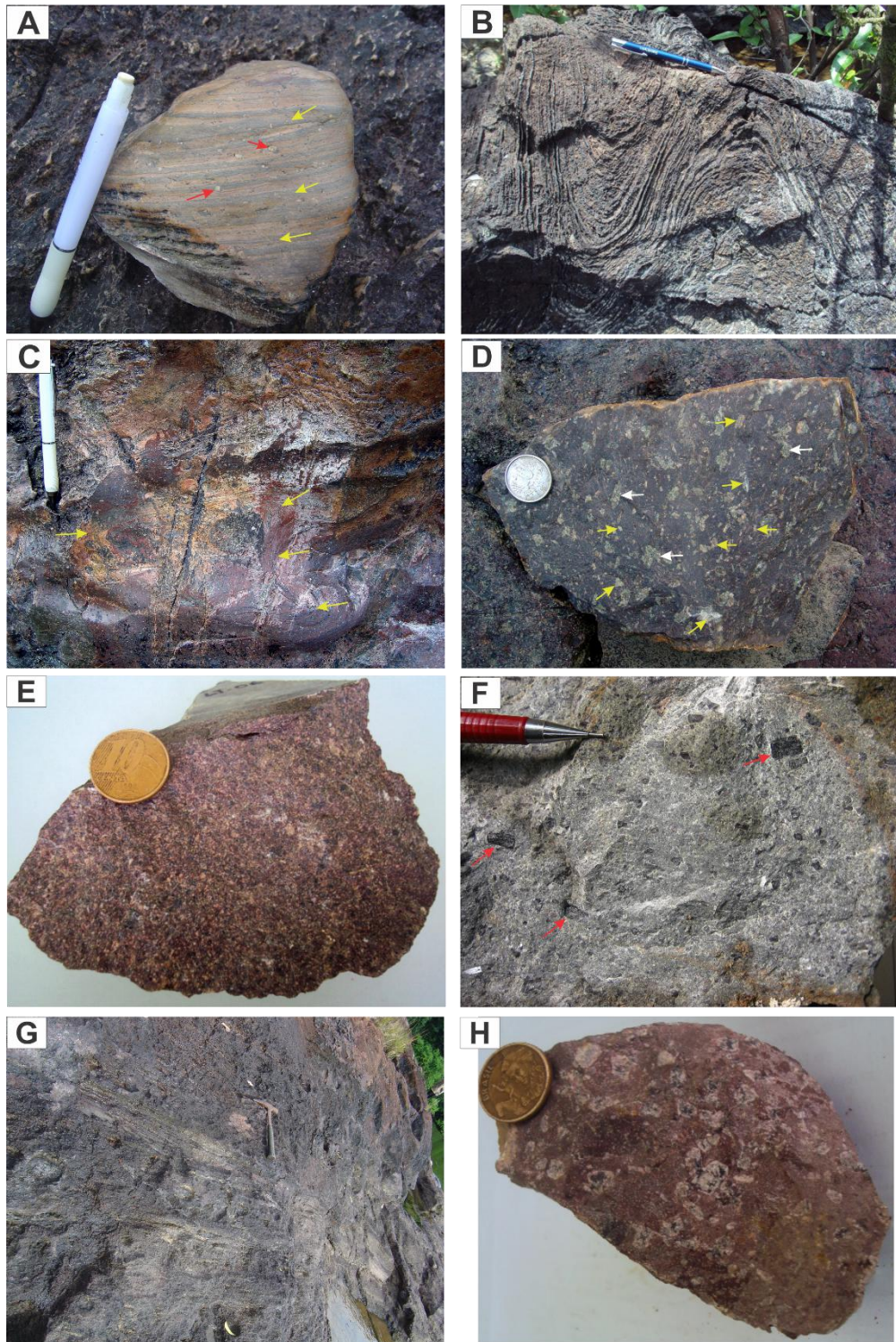
316

317

318

319 **Fig. 3 (below).** Field photographs of the ignimbrites of the Iricoumé Group and Igarapé Paboca Formation.  
320 A-C) Hand-samples showing pumices and fiammes characterizing the eutaxitic and parataxitic textures. The  
321 pumices and fiammes are marked with white arrow (samples LT-22, LT-25, LT-20); D) ignimbrite showing  
322 weak inverse grading (sample LT-22); E) Poorly sorted ignimbrite with ash and lapilli-sized fragments  
323 (sample LT-20); F) Detail of hand-sample showing the crystal fragments of plagioclase, sanidine, and quartz  
324 (yellow arrow), as well as pumices in the groundmass (red arrow) and lithic clasts (red dotted area) (sample  
325 LT-30); G) bands of fiamme devitrified to spherulitic texture. Some spherical spherulites are marked with red  
326 arrow (sample LT-02); H) crystal-rich ignimbrites characterized by high crystal contents of quartz and  
327 feldspar (yellow arrow) and pumices (white arrow) (sample LT-09).





329

330 **Fig. 4.** Field photographs of the explosive and effusive volcanic rocks of the Iricoumé Group and Igarapé Paboca  
331 Formation. A) Bands of rheomorphic ignimbrites characterized by angular-shaped crystal fragments of plagioclase and  
332 fiammes (yellow arrow) characterizing the parataxitic texture (sample LT-25); B) Rheomorphic ignimbrite showing tight  
333 isoclinal folds in field-scale (cf. Silva et al. 2019; sample LT-21); C) Detail of the fiammes and tight isoclinal folds in the  
334 field-scale (yellow arrow) (sample LT-21); D) Rheomorphic ignimbrite showing all fiamme collapsed where the  
335 parataxitic texture is faintly visible, which could led a false interpretation of apparent porphyritic. The crystal fragments  
336 of plagioclase and lithic clasts are highlighted by yellow and white arrows, respectively (sample LT-31); E) Crystal-rich



337 lava with porphyritic texture, characterized by plagioclase and amphibole phenocrysts set in an aphanitic groundmass  
338 (sample LT-06); F) lamprophyre massive and porphyritic, characterized by amphibole phenocrysts (red arrow) set in an  
339 aphanitic matrix (sample LT-11); G) Flow-foliations in hypabyssal dacite (sample LT-08); H) Dacitic rock in hand-  
340 sample exhibiting alkali feldspar and plagioclase porphyries set in an aphanitic groundmass (sample LT-08).

341

## 342 *4.2. Textural analysis*

343 Volcanic rocks were divided into lavas and volcanoclastic facies and accordingly  
344 subdivided into five textural groups with different welding intensities for the pyroclastic  
345 deposits as shown in Table 2 and described below.

346

### 347 *4.2.1. Volcanoclastic facies*

#### 348 ***Apparent porphyritic texture with granophyric groundmass (Incipient degree of welding*** 349 ***- rank I)***

350 The ignimbrites of this category show fragmental texture with low to voluminous (5 to  
351 35 vol.%) poorly sorted angular to sub-rounded fragments of sanidine, plagioclase, and  
352 quartz characterizing an apparent porphyritic texture set in a granophyric groundmass  
353 made up of mosaic of quartz and feldspar (Fig. 5A, 5B). Some quartz fragments in the  
354 ignimbrites exhibit corrosion embayments, which indicate magmatic resorption (Fig. 5C).  
355 Subordinately, there are some samples of ignimbrites with high concentration of crystal  
356 fragments and lithic clasts (Fig. 5A, 5D, 5E).

357 The crystal fragments are set in this groundmass rich in slightly deformed pumice and  
358 devitrified glass shards (Fig. 5A-5E). The pumice fragments have ragged margins, with  
359 lenticular and blocky shapes and are completely altered to phyllosilicate minerals, ensuring  
360 preservation of their outlines (Fig. 5A-5G). Pumices are deformed with flame-like ends,  
361 especially around accidental lithic clasts and crystal fragments, such as quartz, plagioclase,  
362 and biotite (Fig. 5D-5F). Sometimes, the pumices encompass lithic clasts and crystal

363 fragments (Fig. 5E), including biotite crystals completely pseudomorphosed by iron oxides  
364 (Fig. 5D-5E).

365 The glass shards observed in the groundmass are more easily recognized in plane  
366 polarized light and show incipient welding compaction and their shapes range from cusped,  
367 Y-shaped, platy, curvilinear, blade-like, to pumice (Fig. 5C, 5F, 5G). Taking into account  
368 the vitroclastic texture produced by pyroclastic eruptions is no longer preserved in the  
369 matrix of these Precambrian ignimbrites, all the shapes of the shards were well preserved  
370 due to devitrification to fine-grained quartz-feldspar aggregates (Fig. 5G).

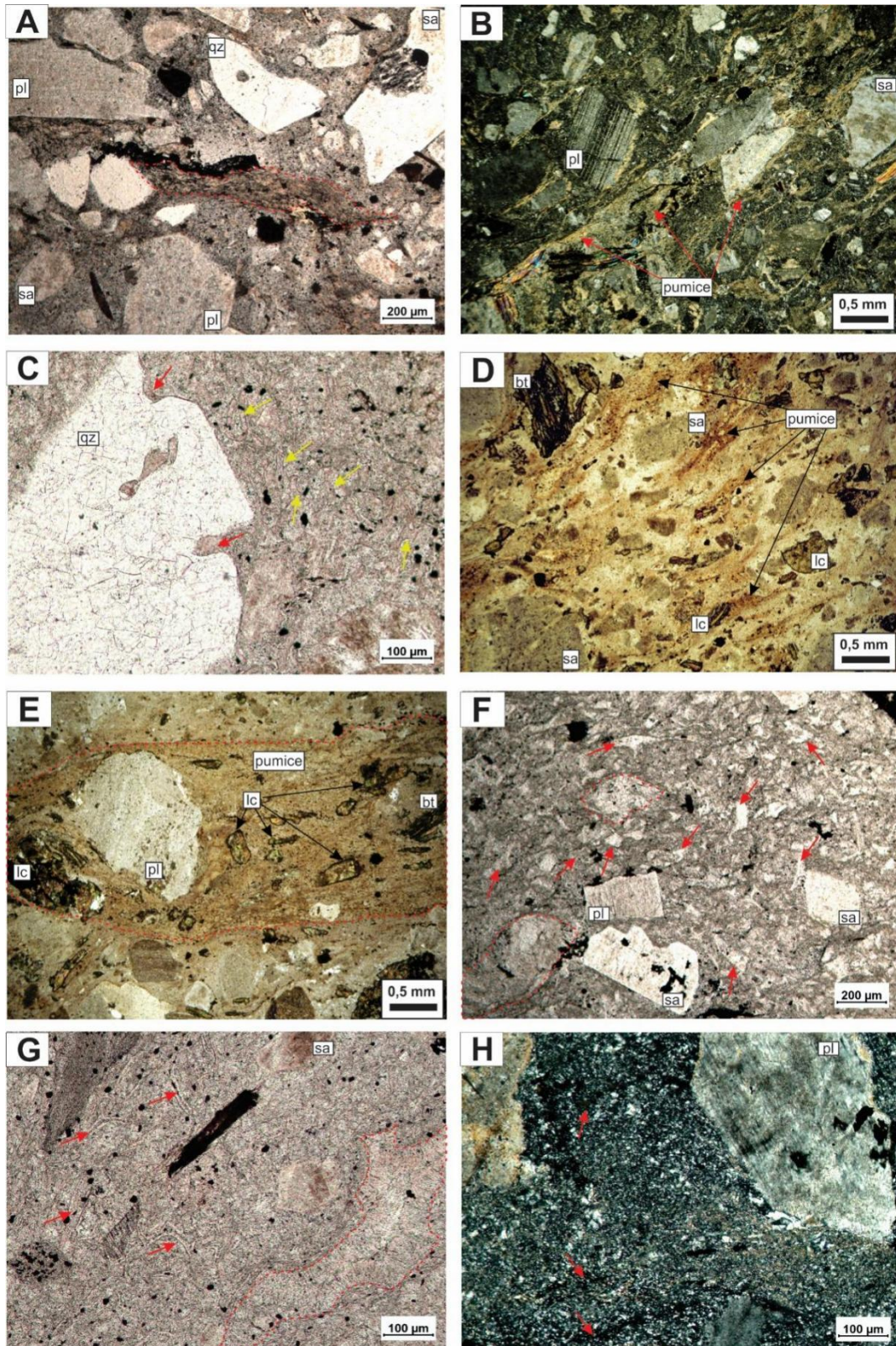
371 The granophyric texture was also described in the groundmass and is characterized by  
372 fine-grained amorphous quartz (cristobalite) and feldspar aggregates (Fig. 5B, 5H). This  
373 granophyric texture commonly overprints any pre-existing vitroclastic texture in the matrix  
374 and is the result of high-temperature devitrification processes as well as the spherulitic  
375 texture that is also present (Fig. 5G).

376 According to the incipiently welded texture of the pumices, these rocks belong to rank  
377 I in the welding intensity, which is equivalent to grades II and III of classification of Quane  
378 and Russel (2004).

FACIES	SAMPLE	TEXTURAL CATEGORY	RANK		WELDING INTENSITY	INTERPRETATION OF PROCESS	FIGURES		
			Literature <sup>1</sup>	This study					
VOLCANICLASTIC			I						
	LT-09	Apparent porphyritic with cryptocrystalline groundmass	II	I	The glass shards are only slightly deformed. The pumices are incipiently flattened and welded and no eutaxitic texture is observed. The glassy material (shards and pumices) are completely devitrified	The weak deformation of pyroclasts suggests the beginning of the welding in the ash matrix and pumice lapilli and a pyroclastic origin for these deposits <sup>2</sup>	3F,3H, 5A-5H		
	LT-12								
	LT-29								
	LT-03*								
	LT-20								
	LT-30	Eutaxitic	IV	II	The glass shards are moderately adhered to one another and individual shards are moderately deformed. Rocks moderately to strongly welded with a clear eutaxitic texture showing moderately deformed pumices as well as fully collapsed fiamme	The eutaxitic texture record hot deformation of pyroclasts and is generated by increasing welding process involving syn or post-emplacment degassing, compaction, annealing and flow of glassy material in pyroclastic deposits <sup>2</sup>	Fig. 3A, 3D, 3G, 6A-6F		
	LT-21								
	LT-22								
	LT-18								
	LT-01	Parataxitic	V	III	densely welded with all fiamme collapsed. The strong eutaxitic texture change for parataxitic texture with features of folds, elongation lineations and boudins. Sometimes the obsidian-like fiamme are faintly visible or difficult to identify that resembles to texture of a lava	The parataxitic texture is formed when all the fiammes of a pyroclastic deposit suffer coalescence and are welded to obsidian-like vitrophyre, which remove the pore spaces. Development of pronounced elongation lineations, folds, kinematic indicators, and boudins indicate syn- and/or postwelding hot-state ductile shear deformation (process of reomorphism) <sup>2</sup>	Fig. 3B, 3C, 4A-4D, 7A-7F		
	LT-16								
	LT-25		VI						
	LT-31*								
COHERENT	LT-06*	Porphyritic and glomeroporphyritic with microcrystalline to pilotassitic groundmass				The porphyritic and glomeroporphyritic textures suggest emplacement of lava flows with crystallization in two stages and heterogeneous crystallization, respectively. The microcrystalline to pilotassitic textures of the groundmass indicate lack to intermediate movement of flow of the lava flows <sup>3</sup>	Fig. 4E, 4F, 8A, 8B, 8C, 8D		
	LT-04*								
	LT-24								
	LT-11								
	LT-08	Porphyritic and glomeroporphyritic with spherulitic groundmass						The porphyritic and glomeroporphyritic textures suggest emplacement of lava flows with crystallization in two stages and heterogeneous crystallization, respectively. The spherulitic texture of the groundmass indicate high-temperature devitrification <sup>3</sup>	Fig. 4G, 4H, 8E, 8F
	LT-26								

379

380 **Table 2.** Summary of textural categories and rank of welding intensities of the volcanic rocks of the Iricoumé Group and Igarapé Paboca Formation. 1= Quane and  
381 Russel (2004); \*= samples from the Igarapé Paboca Formation; 2= Branney and Kokelaar (2002); 3= Vernon (2004).



382

383 **Fig. 5.** Photomicrographs of the incipiently welded apparent porphyritic texture, which represents the  
384 rank I of the welding intensity. A) Crystal-rich ignimbrite characterized by angular fragments of plagioclase  
385 (pl), sanidine (sa) and quartz (qz) set in a groundmass with pumices (red dotted area) incipiently welded  
386 (sample LT-09) - Parallel polarized light; B) Crystal-rich ignimbrite with fragmental texture and poorly

387 sorted angular fragments of sanidine (sa) and plagioclase (pl) set in granophyric groundmass with slightly  
388 deformed pumice and altered to phyllosilicates (sample LT-12) – Crossed polarized light; C) Ignimbrite  
389 showing quartz fragment with corrosion embayment (red arrow) set in a groundmass with glass shards  
390 (yellow arrows) (sample LT-03) – Parallel polarized light; D) Pumice fragments show lenticular shapes and  
391 ragged margins deformed around sanidine crystals (sa) and lithic clasts (lc) and are completely altered to  
392 phyllosilicate minerals, ensuring preservation of their outlines. Biotite crystals are completely  
393 pseudomorphosed by iron oxides (sample LT-29) – Parallel polarized light; E) Pumices with blocky shape  
394 that encompass accidental lithic clasts (lc), plagioclase (pl) and biotite (bt) fragments (sample LT-29) –  
395 Parallel polarized light; F) Ignimbrite with poorly sorted fragmental texture defined by angular to sub-  
396 rounded fragments of sanidine (sa) and plagioclase (pl) in a groundmass rich in shards with shapes ranging  
397 from cusped, Y-shaped, platy, curvilinear (red arrow), to pumice (red dotted area) (sample LT-20) – Parallel  
398 polarized light; G) Detail of the well preserved outlines of the glass shards (red arrow) and spherulitic texture  
399 (red dotted area) in the matrix (sample LT-03) – Parallel polarized light; H) Pumice fragments (red arrow)  
400 and granophyric texture in the groundmass, characterized by fine-grained quartz-feldspar aggregates (sample  
401 LT-20) – Crossed polarized light.  
402

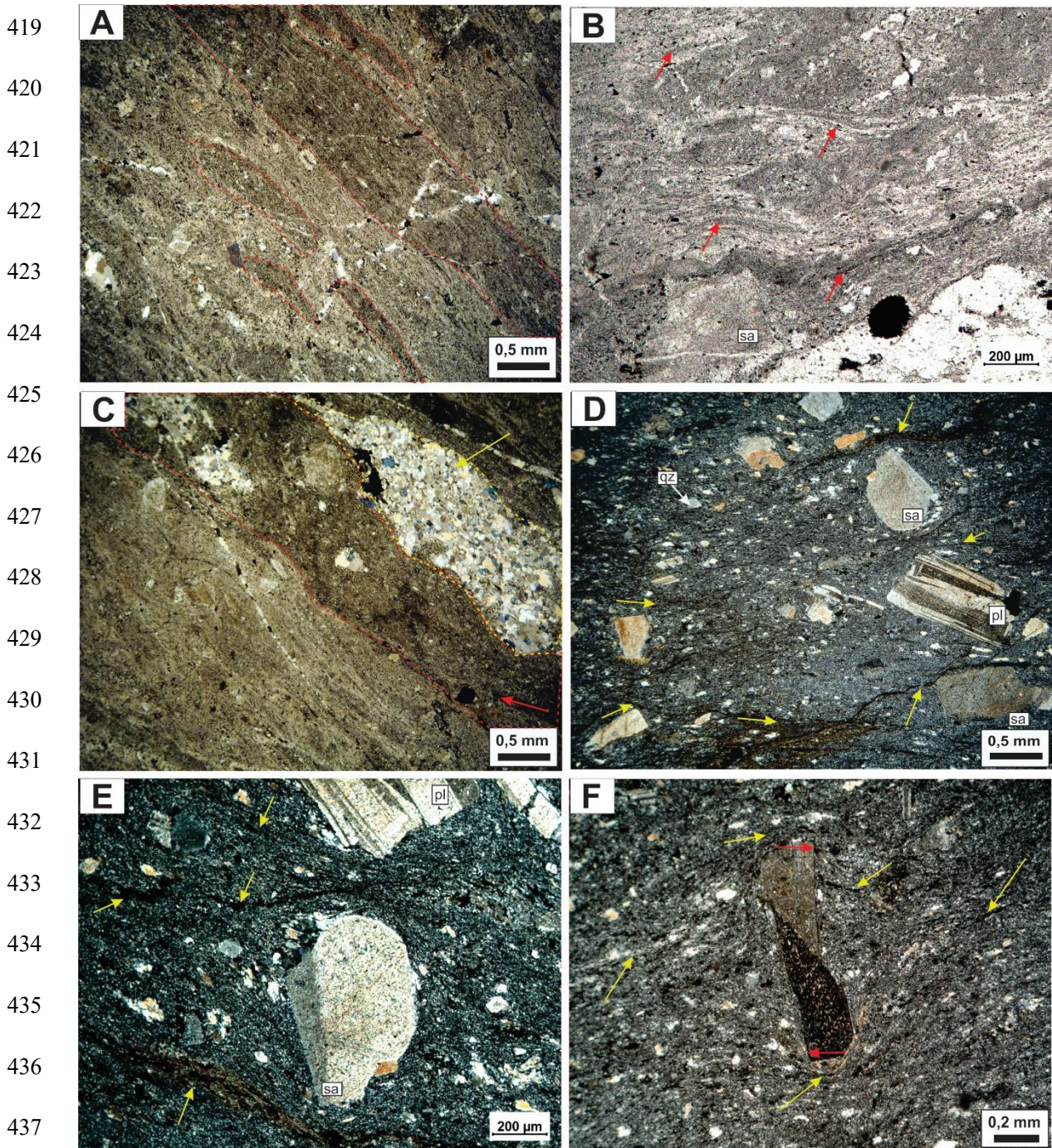
#### 403 ***Eutaxitic texture (moderate degree of welding - rank II)***

404 Ignimbrites exhibit discontinuous foliation that alternates from light to dark colors,  
405 which reflects welding on different materials (Fig. 6A-6B). The ignimbrites are composed  
406 mainly of crystal fragments of sanidine, plagioclase, quartz, biotite, and strongly flattened  
407 fiamme fragments characterizing an eutaxitic texture (Fig. 6A-6E). Lenticular to disc-  
408 shaped fiamme have wispy, flame-like ends and are deformed, especially around rigid  
409 components (crystal fragments) (Fig. 6C-6F), in which some crystal fragments are rotated  
410 (Fig 6F). Lithic clasts are scarce in these ignimbrites.

411 The processes that obliterate the vitroclastic texture include high welding degree and  
412 alteration of fiamme to phyllosilicate minerals and quartz-feldspar aggregates (Fig. 6C).  
413 Features of high-temperature devitrification are also observed generating the granophyric  
414 texture that comprises a fine-grained quartz-feldspar mosaic (Fig. 6D-6F).

415 Based on the eutaxitic texture of these ignimbrites that characterizes a moderate degree  
416 of welding of the pumices towards fiammes, these rocks are classified in the rank II of the

417 welding intensity, which is equivalent to grade IV of classification of Quane and Russel  
418 (2004).



438 **Fig. 6.** Photomicrographs of ignimbrites with eutaxitic texture, which represent the rank II of welding  
439 intensity. A) Ignimbrite with discontinuous foliation characterized by lenticular to disc-shaped fiammes (dark  
440 colors highlighted by red dotted line) (sample LT-21) – Parallel polarized light; B) Fiammes (red arrow)  
441 with lenticular shapes and sometimes deformed around sanidine (sa) fragment (sample LT-21) – Parallel polarized  
442 light; C) Fiammes altered to phyllosilicate minerals (red arrow) and quartz-feldspar aggregates (yellow arrow)  
443 (sample LT-21) – Parallel polarized light; D) Ignimbrite with crystal fragments of sanidine (sa), plagioclase

444 (pl), quartz (qz), and strongly flattened fiammes characterizing the eutaxitic texture. Fiammes (yellow arrow)  
445 altered to phyllosilicates have flame-like ends and are deformed around crystal fragments (sample LT-18) –  
446 Crossed polarized light; E) Detail of the angular plagioclase (pl) and sanidine (sa) fragments rounded by  
447 fiammes deformed. Groundmass completely devitrified to fine-grained quartz-feldspar mosaic characterizing  
448 the granophyric texture is also present (sample LT-18) – Crossed polarized light; F) Detail of the rotated  
449 plagioclase fragment (red arrow) wrapped by fiammes altered to phyllosilicate (yellow arrow) (sample LT-18)  
450 – Crossed polarized light.

451

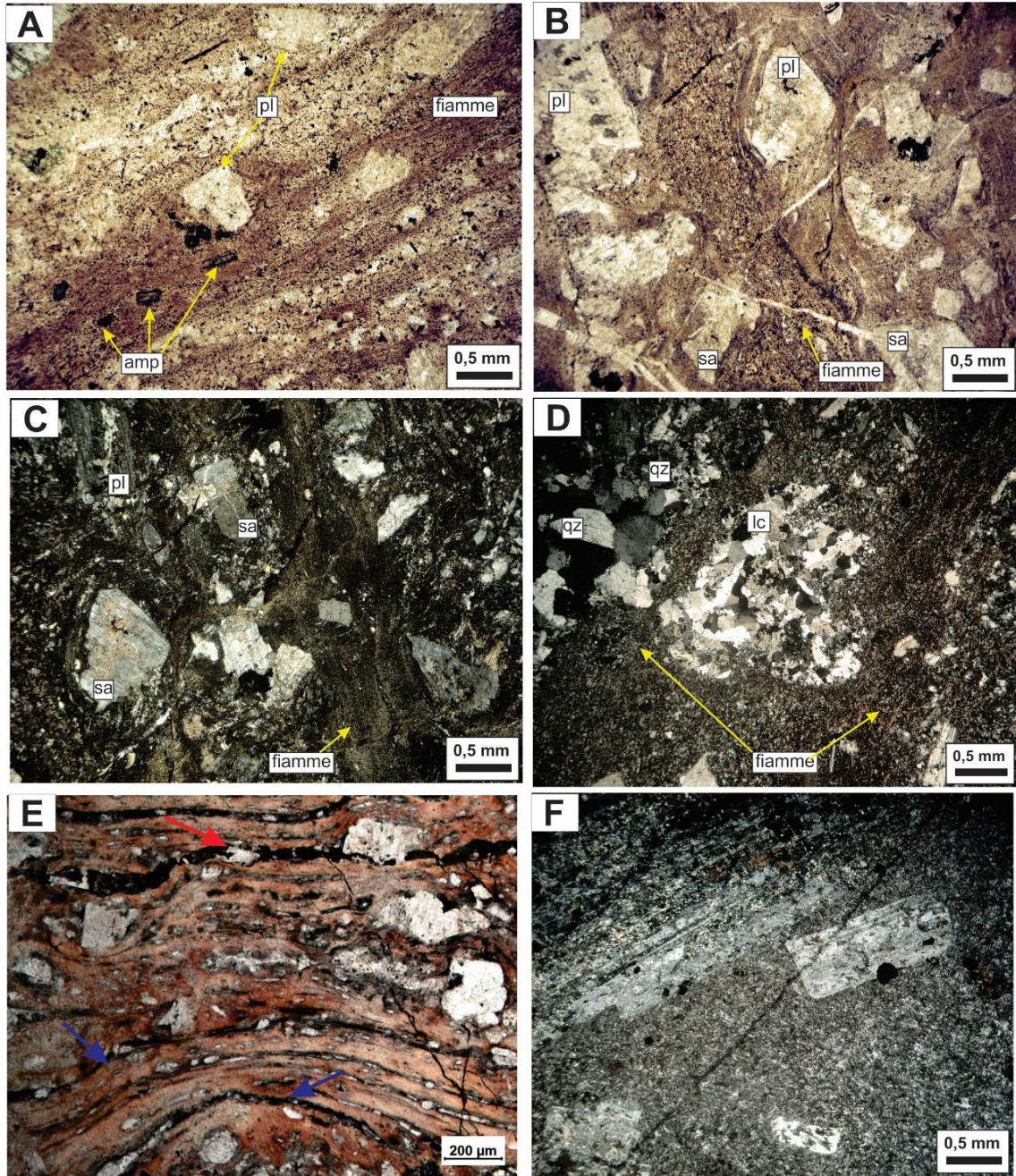
### 452 ***Parataxitic texture (high welding degree - rank III)***

453 The rheomorphic ignimbrites are characterized by broken crystal fragments of sanidine,  
454 plagioclase, quartz, and amphibole within groundmass with densely welded fiammes that  
455 are difficult to distinguish (Fig. 7A-7F). These ignimbrites commonly display high-  
456 temperature devitrification of the formerly glassy components generating granophyric  
457 textures (Fig. 7C, 7D, 7F).

458 The amphibole crystals are partially to completely replaced by opaque minerals (Fig.  
459 7A). The fiamme fragments show a reddish color due to oxidation (Fig. 7A, 7B, 7E) and  
460 are deformed and flattened around crystal fragments and cognate and accidental lithic  
461 clasts (Fig. 7A-7E).

462 The foliations developed in the rheomorphic ignimbrites define the parataxitic texture,  
463 characterized by strong welding and compaction of fiamme, which generate intrafolial  
464 folds in micro-scale and boudinage features (Fig. 7E), suggesting that the rheomorphic  
465 processes occurred during and/or after flow emplacement (Branney and Kokelaar, 2002).  
466 In most cases, this strong welding and compaction approaching homogenization generates  
467 a pattern of structures similar to magmatic foliations, typical of lavas (Fig. 7F).

468 Based on the parataxitic texture described in the rheomorphic ignimbrites, these rocks  
469 are classified in the rank III of the welding intensity, which is equivalent to grade V and VI  
470 of the classification of Quane and Russel (2004).



471

472 **Fig. 7.** Photomicrographs of rheomorphic ignimbrite with parataxitic texture, which represent the rank III of  
473 welding intensity. A-B) Broken crystal fragments of sanidine (sa), plagioclase (pl), and opaque-altered  
474 amphibole (amp) within groundmass with densely welded fiammes that are difficult to distinguish. The  
475 fiamme fragments show a reddish tint in plane-polarized light due to oxidation and are deformed and  
476 flattened around lithic clasts and crystal fragments (samples LT-01 and LT-16) – Parallel polarized light; C-D)  
477 Strongly welded fiammes around crystal fragments of plagioclase (pl), sanidine (sa) and quartz (qz), and  
478 lithic clasts (lc). Note the granophytic texture in the devitrified groundmass (samples LT-01 and LT-16) –  
479 Crossed polarized light; E) The strong welding and compaction of fiammes (dark due to limited transparency



480 under a petrological microscope) generate intrafolial folds in micro-scale (blue arrow) and boudinage features  
481 (red arrow) (sample LT-25) - Parallel polarized light; F) The strong welding and compaction of the  
482 rheomorphic ignimbrites led to the approaching homogenization generating a pattern of textures similar to  
483 magmatic foliations, typical of lavas. Note the granophytic texture in the devitrified groundmass (sample LT-  
484 31) – Crossed polarized light.

485

#### 486 4.2.2. Lavas

#### 487 *Porphyritic and glomeroporphyritic texture with microcrystalline to pilotaxitic* 488 *groundmass*

489 The andesitic lavas and hypabyssal lamprophyres of andesitic composition show  
490 porphyritic and glomeroporphyritic textures characterized by 30-50% (vol.) of phenocrysts  
491 set in a groundmass of high crystallinity (Fig. 8A-8D).

492 The lavas show voluminous (35-50% vol.) phenocrysts of plagioclase and hornblende  
493 immersed in a microcrystalline groundmass, where predominate plagioclase microlites and  
494 small crystals of hornblende (Fig. 8A). All plagioclase crystals exhibit subhedral shapes  
495 and are moderately to strongly replaced by clay minerals, carbonate, and epidote.  
496 Hornblende phenocrysts show subhedral to sub-rounded shapes and are partially to  
497 completely replaced by opaque minerals (Fig. 8B).

498 The lamprophyres exhibit hornblende phenocrysts that reach up to 30% (vol.) set in a  
499 pilotaxitic groundmass, characterized by plagioclase microlites aligned in sub parallel  
500 mode along with hornblende microphenocrysts (Fig. 8C). Hornblende phenocrysts show  
501 subhedral to sub-rounded shapes, sometimes as aggregates in addition to zoning, simple  
502 twinning, and opacitic rims (Fig. 8C). Some crystals are partially to completely replaced by  
503 chlorite and opaque minerals, while others are partially corroded (Fig. 8D). All plagioclase  
504 crystals show subhedral shapes and are slightly replaced by clay minerals and epidote. The

505 fact that these lamprophyres exhibit hornblende as the only mafic mineral and  
506 plagioclase > alkali feldspar (Le Maitre, 2002) allows classify them as spessartite.

507

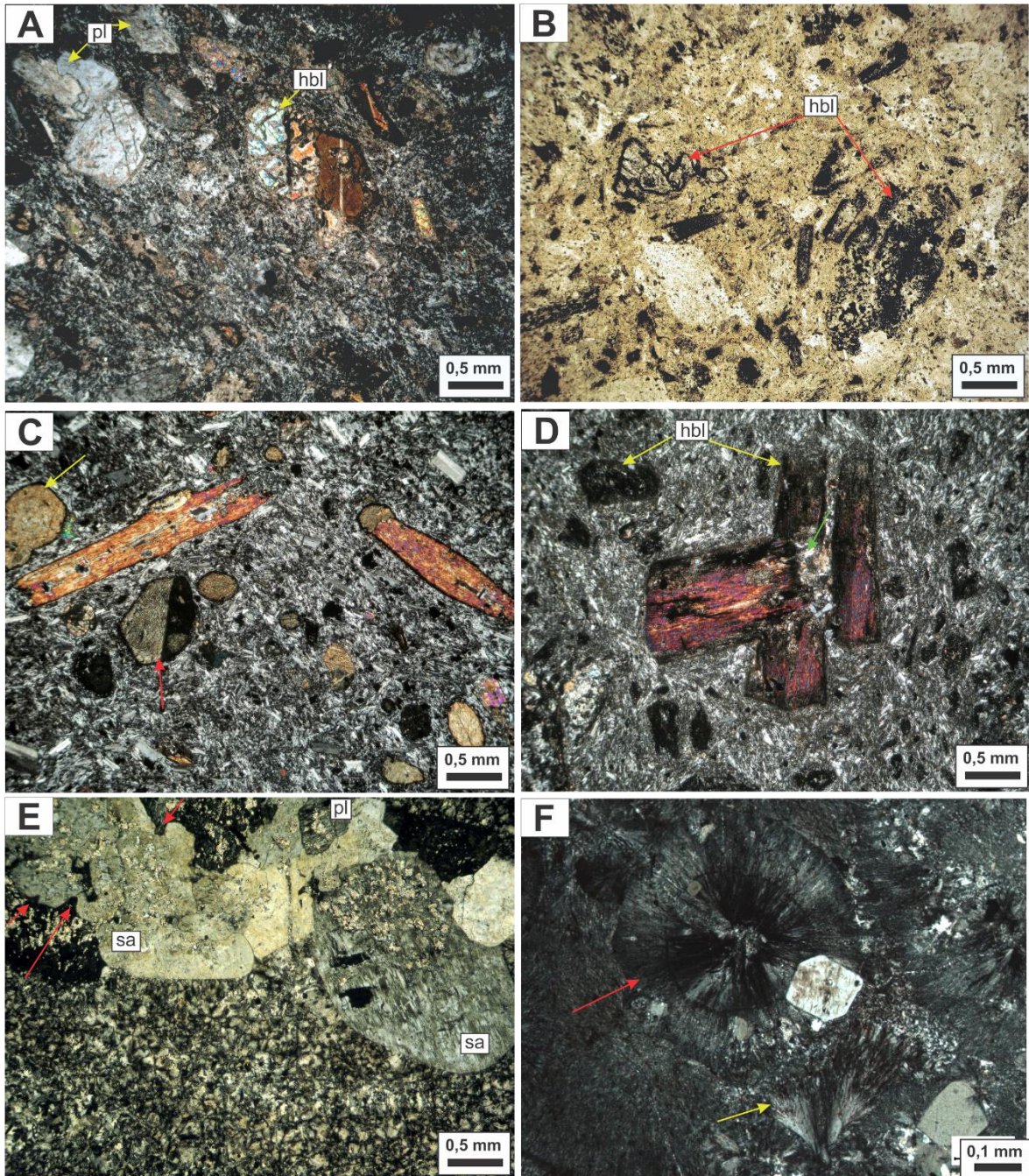
508 ***Porphyritic and glomeroporphyritic texture with spherulitic groundmass***

509 The dacitic subvolcanic rocks show porphyritic and glomeroporphyritic textures,  
510 characterized by plagioclase, quartz, and sanidine phenocrysts immersed in a glassy matrix  
511 (Fig. 8E-8F).

512 The plagioclase phenocrysts show shapes ranging from subhedral to euhedral and are  
513 partially altered to sericite, carbonate, and clay minerals. The sub-rounded sanidine  
514 porphyry exhibit carlsbad twinning, microperthites and are slightly- to moderately altered  
515 to sericite (Fig. 8E). Features of corrosion embayment are observed in the quartz and  
516 sanidine phenocrysts as a result of partial reabsorption processes (Fig. 8E). The matrix has  
517 undergone high-temperature devitrification processes generating spherulitic texture with  
518 axiolite, spherical, and fan-type spherulites (Fig. 8F).

519

520 **Fig. 8 (below).** Textural groups of the effusive deposits. A) Lava showing porphyritic texture  
521 characterized by plagioclase and hornblende phenocrysts immersed in a microcrystalline groundmass  
522 composed by plagioclase microlites and small crystals of hornblende (sample LT-24) – Crossed polarized  
523 light; B) Hornblende phenocrysts of the lavas show subhedral to sub-rounded shapes and are partial to  
524 completely altered for opaque minerals (sample LT-06) – Parallel polarized light; C) Lamprophyre exhibit  
525 porphyritic texture defined by hornblende phenocrysts set in a pilotassitic groundmass, characterized by  
526 plagioclase microlites aligned in sub parallel mode. Hornblende phenocrysts with subhedral to sub-rounded  
527 shapes show zoning (yellow arrow), simple twinning (red arrow), and opacitic rims (sample LT-04) –  
528 Crossed polarized light; D) Most of the hornblende phenocrysts range from partially to completely replaced  
529 by opaque minerals (yellow arrow), while some are partially corroded (green arrow) (sample LT-11) –  
530 Crossed polarized light; E) Hypabyssal dacite with glomeroporphyritic texture composed by plagioclase (pl)  
531 and microperthitic sanidine (sa) porphyries with sub-rounded shapes and corrosion embayment (red arrow)  
532 set in a spherulitic groundmass (sample LT-08) – Crossed polarized light; F) Detail of the fan (yellow arrow)  
533 and spherical-type (red arrow) spherulites scattered in the spherulitic groundmass (sample LT-26) – Crossed  
534 polarized light.



535

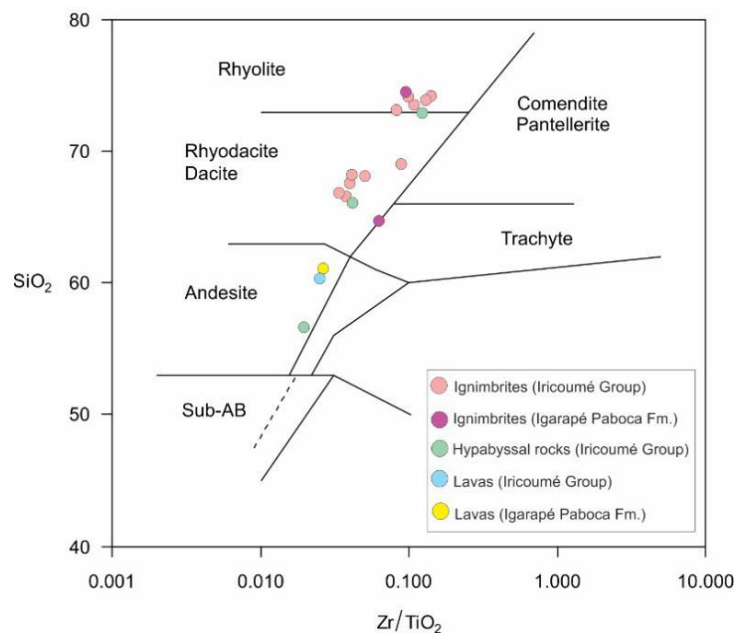
536

### 537 4.3. Geochemistry

538 Eighteen volcanic rocks representative of the Iricoumé Group and Igarapé Paboca  
539 Formation were analyzed for whole-rock geochemistry, including 13 ignimbrites, two  
540 lavas, and three hypabyssal rocks (Table 3). From this set, most of the samples are related

541 to the Iricoumé Group, except by two pyroclastic rocks (samples LT-03 and LT-31) and  
542 one lava (sample LT-06) that belong to Igarapé Paboca Formation and are marked with an  
543 asterisk in table 2.

544 Barreto et al. (2014) described in detail the geochemical characteristics of major and  
545 trace elements of the volcanic rocks of this sector of the Erepecuru-Trombetas Domain.  
546 The high values of Loss on Ignition (LOI) obtained in some studied rocks (c.f. Table 2 of  
547 Barreto et al., 2014) due to weathering did not allow their classification in the Total-Alkali  
548 ( $\text{Na}_2\text{O} + \text{K}_2\text{O}$ ) versus silica (TAS) diagram, as recommended by the International Union of  
549 Geological Sciences (IUGS). As a better alternative for the classification of altered  
550 volcanic rocks, we used the  $\text{Zr}/\text{TiO}_2$  versus  $\text{SiO}_2$  diagram (Winchester and Floyd, 1977)  
551 that establishes a relationship between major and trace elements with low degree of  
552 mobility (Fig. 9). In this diagram, the pyroclastic rocks occupy the dacite and rhyolite  
553 fields, while the lava domes show andesitic composition and the hypabyssal rocks range  
554 from andesitic to dacitic compositions.



555

556 **Fig. 9.**  $\text{SiO}_2$  versus  $\text{Zr}/\text{TiO}_2$  classification diagram (Winchester and Floyd, 1977). Fm.= Formation. The  
557 pyroclastic rocks of the Igarapé Paboca Formation are the purple circles, while the lava of this unit is  
558 represented by yellow circle.

559 4.4. Temperature and viscosity of magmas

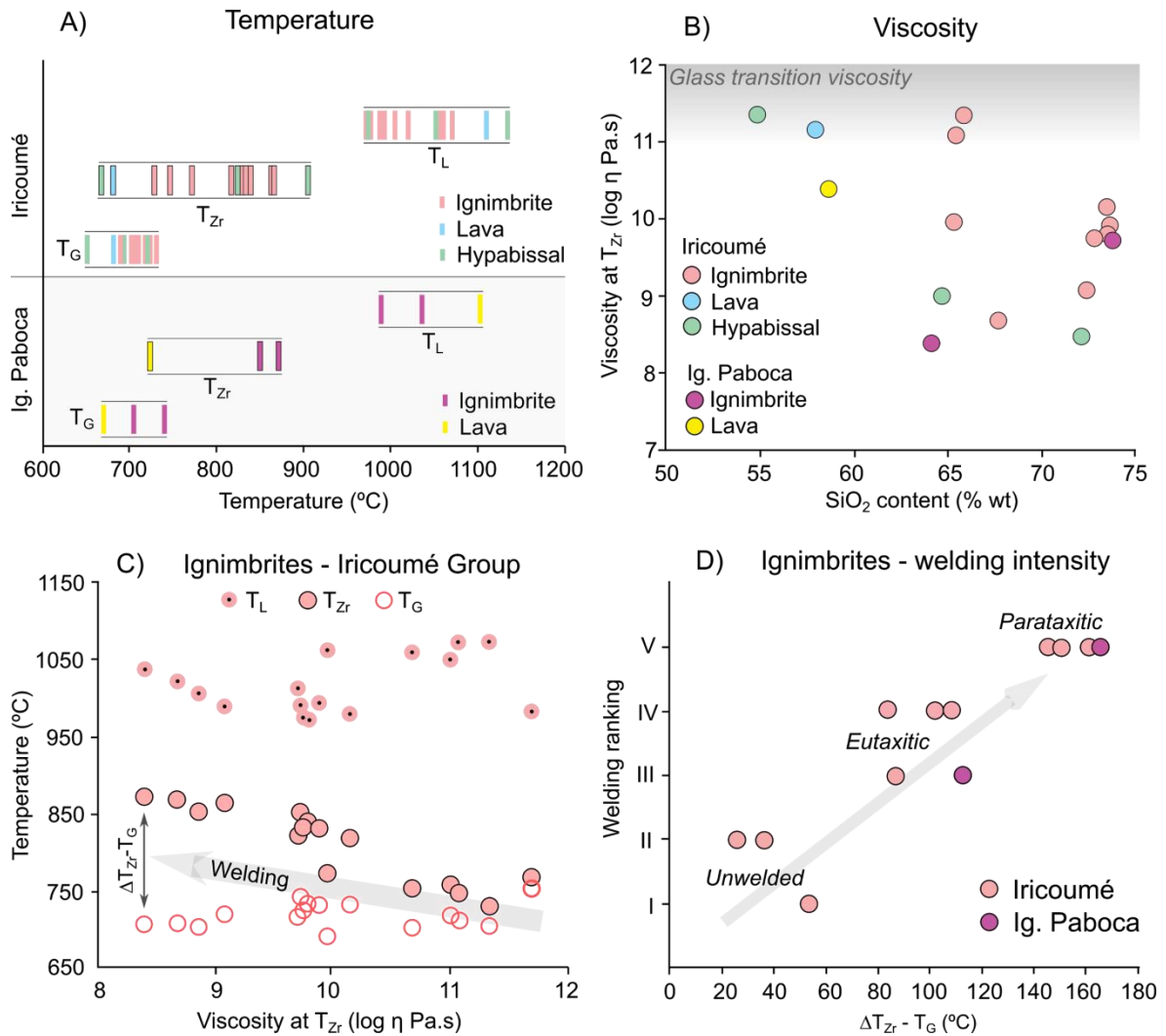
560 The main rheological parameters calculated on basis in the geochemical data are  
561 shown in the Table 3. Our results indicate that, for anhydrous compositions, Iricoumé  
562 Group melts present uniform  $T_L$  ranging from 920 to 1110 °C (average of 1020 °C),  
563 without significant  $T_L$  differences among explosive and effusive samples (Fig. 10A).  
564 Overall, samples of the Igarapé Paboca Formation display higher temperatures, with an  
565 average  $T_L$  of 1050 °C (Fig. 10A). Zircon saturation temperatures ( $T_{Zr}$ ) of Iricoumé Group  
566 display large variations from 707 to 905 °C (average of 810 °C, Fig. 10A).

567 The calculated viscosities at  $T_{Zr}$  span from 8.4 to 11.7 log  $\eta$  (Pa.s) (Fig. 10B),  
568 indicative of the *non-Arrhenius* behavior of these melts (Giordano et al., 2006). Comparing  
569 samples with similar silica content (SiO<sub>2</sub> % wt), several explosive samples tend to show  
570 significantly higher viscosities at  $T_{Zr}$  when compared to effusive samples (Fig. 10B). This  
571 difference can reach two orders of magnitude (i.e., 100 more viscous) in some cases.

572 When considering only pyroclastic samples of the Iricoumé Group, it is possible to  
573 observe high, virtually uniform  $T_L$ , and variable  $T_{Zr}$ , ranging from 729 to 871 °C, while  $T_G$   
574 ranges from 690 to 753 °C (Fig. 10C). In the pyroclastic samples of Iricoumé Group, the  
575  $\Delta T_{Zr} - T_G$  ranges from 14 to 165 °C (Fig. 10D), with several samples (> 70%) presenting  
576 high  $\Delta T_{Zr} - T_G$  values (> 80 °C), indicative of a high welding potential for the pyroclastic  
577 deposits of the Iricoumé Group. Explosive samples from the Igarapé Paboca Formation  
578 also display high  $\Delta T_{Zr} - T_G$  values, which is attested by moderate to intense welding  
579 observed in these samples (Fig. 10D). This proxy also indicates that some samples were  
580 emplaced only a few degrees above the glass transition temperature, generating unwelded  
581 deposits. When compared to petrographic data and the ranking welding intensity based on  
582 the modified scale from Quane and Russell (2004), pyroclastic samples show a systematic

583 increase in welding intensity as a function of  $\Delta T_{Zr} - T_G$  (Fig. 10D), suggesting the ability of  
 584 the  $\Delta T_{Zr} - T_G$  proxy in predicting welding degree in the pyroclastic samples.

585



586

587 **Fig. 10.** Rheological results for Iricoumé and Igarapé Paboca melts: A) temperature results for the  
 588 studied units,  $T_L$ ,  $T_{Zr}$  and  $T_G$ ; B) melt viscosity at  $T_{Zr}$  versus silica content; C)  $T_{Zr}$  and  $T_G$  versus melt  
 589 viscosity of explosive samples from Iricoumé Group; D) petrographic welding ranking versus welding  
 590 potential for ignimbrites of the Iricoumé Group and the Igarapé Paboca Formation. Geochemical data from  
 591 Barreto et al. (2014) and partly displayed in the table 3.

592

593

594

Identification		Main network forming		Main network modifiers			Anydrous (0% H <sub>2</sub> O)						0.25% H <sub>2</sub> O			0.50% H <sub>2</sub> O			1.00% H <sub>2</sub> O			2.00% H <sub>2</sub> O			4.00% H <sub>2</sub> O		
Type	Sample	SiO <sub>2</sub>	Al <sub>2</sub> O <sub>3</sub>	Na <sub>2</sub> O	K <sub>2</sub> O	P <sub>2</sub> O <sub>5</sub>	Zr (ppm)	TL (°C)	log η at TL (Pa.s)	T Zr (°C)	log η at T Zr (Pa.s)	TG (°C)	TL (°C)	log η (Pa.s)	TG (°C)	TL (°C)	log η (Pa.s)	TG (°C)	TL (°C)	log η (Pa.s)	TG (°C)	TL (°C)	log η (Pa.s)	TG (°C)	TL (°C)	log η (Pa.s)	TG (°C)
Explosive (Pyroclastic)	LT-01 (D)	67.48	15.96	4.47	6.17	0.19	288	1005	6.67	852	8.85	702	996	6.00	636	988	5.63	594	971	5.19	537	938	4.68	462	872	4.14	363
	LT-09 (D)	66.25	15.24	5.00	3.54	0.18	149	1058	5.81	753	10.67	701	1050	5.24	638	1041	4.91	596	1025	4.52	542	991	4.09	471	925	3.64	380
	LT-12 (D)	65.45	15.59	4.43	3.61	0.18	141	1071	5.76	747	11.08	711	1063	5.18	648	1055	4.87	608	1038	4.48	553	1005	4.04	482	939	3.60	391
	LT-16 (D)	67.69	15.27	4.56	5.48	0.11	451	1020	6.54	867	8.68	707	1011	5.89	641	1003	5.54	600	987	5.10	543	953	4.60	468	887	4.08	371
	LT-29 (D)	65.84	15.73	4.72	3.72	0.20	127	1071	5.62	729	11.33	704	1063	5.05	640	1055	4.74	601	1038	4.36	546	1005	3.94	476	939	3.51	388
	LT-30 (D)	65.31	15.35	4.65	4.39	0.21	157	1061	5.55	772	9.96	690	1053	5.00	627	1045	4.69	586	1028	4.32	533	995	3.91	464	929	3.49	375
	LT-31 (T)*	64.11	16.13	3.78	5.96	0.29	507	1036	6.07	871	8.40	706	1027	5.44	641	1019	5.11	601	1003	4.70	546	970	4.25	475	903	3.79	384
	LT-03 (R)	73.78	13.72	3.35	5.42	0.04	279	989	7.63	851	9.71	740	980	6.91	674	972	6.50	631	956	6.01	572	922	5.44	494	856	4.83	390
	LT-18 (R)	73.64	13.88	4.38	4.26	0.05	237	992	7.41	830	9.88	730	983	6.71	663	975	6.31	621	959	5.83	563	925	5.28	485	859	4.69	382
	LT-20 (R)	73.48	14.60	4.51	3.95	0.03	184	978	7.58	817	10.14	731	970	6.86	665	962	6.45	623	945	5.96	564	912	5.39	486	846	4.79	383
	LT-21 (R)	73.51	13.58	3.50	5.54	0.02	248	972	7.71	838	9.78	732	963	6.98	665	955	6.57	623	939	6.07	564	906	5.50	486	839	4.90	383
	LT-22 (R)	72.82	13.71	4.40	4.47	0.04	240	974	7.54	831	9.75	724	966	6.82	657	958	6.43	616	941	5.93	558	908	5.37	479	842	4.78	377
LT-25 (R)	72.43	14.30	4.74	4.81	0.05	330	988	7.27	863	9.07	718	980	6.57	651	971	6.18	609	955	5.71	551	922	5.16	473	855	4.57	370	
Effusive (Hypabyssal)	LT-11 (A)	54.86	14.57	4.50	2.03	0.45	155	1134	3.08	668	11.37	652	1125	2.71	595	1117	2.53	561	1101	2.32	518	1068	2.15	468	1001	2.10	411
	LT-08 (D)	72.09	14.74	4.16	5.72	0.04	434	974	7.51	905	8.47	721	966	6.79	654	958	6.38	612	941	5.89	553	908	5.33	475	842	4.72	371
	LT-26 (D)	64.67	16.23	4.96	4.38	0.23	270	1052	5.72	825	8.99	694	1044	5.15	631	1035	4.82	590	1018	4.43	535	986	4.00	465	919	3.56	375
Effusive (Lava)	LT-06 (A)	58.66	15.31	4.97	3.41	0.37	183	1104	4.33	724	10.41	671	1096	3.86	610	1087	3.61	572	1071	3.31	523	1038	3.01	462	972	2.74	387
	LT-24 (A)	57.90	15.45	3.83	3.71	0.36	176	1110	4.24	707	11.19	682	1101	3.78	621	1093	3.53	585	1077	3.24	536	1043	2.96	477	977	2.73	406

**Table 3.** Table of some major elements and zr trace element already published by Barreto et al. (2014) and the summary of the main rheological parameters of the Iricoumé Group and Igarapé Paboca Formation rocks (present study). Composition: Andesite (A), Dacite (D), Rhyolite (R), Trachyte (T).

595  
596  
597

598 **5. Discussion**

599 *5.1. Eruptive dynamics*

600 The methodology applied in this study allowed us to establish a set of diagnostic  
601 features that can be used to distinguish between volcanoclastic and coherent textural  
602 samples generated by explosive and effusive eruptive styles. The explosive deposits are  
603 largely dominant in the studied region and include slightly welded to rheomorphic  
604 ignimbrites.

605 The pyroclastic deposits present massive and stratified aspect and are composed of  
606 devitrified juvenile components (pumice, fiamme, and glass shards), and lithic clasts, and  
607 crystal fragments transported predominantly by pyroclastic density currents (PDCs) during  
608 explosive events (Manville et al., 2009) (Figs. 5-7). PDCs consist of gravity-driven  
609 mixtures of hot gas and volcanic particles (Branney and Kokelaar, 2002), and the  
610 alternation of massive and stratified deposits is a common characteristic in PDC deposits  
611 (Sulpizio et al., 2014). This arrangement reflects primary events of deposition of  
612 concentrated PDCs, dominated by granular flow regimes (Sulpizio et al., 2014). The  
613 presence of devitrified juvenile components represent an important textural feature to  
614 distinguish silicic lavas from ignimbrites in the ancient volcanic environment of the  
615 Amazonian Craton (Figs. 5F, 5G, 6C-6E).

616 In contrast, the effusive eruptive style responsible for the coherent textures is  
617 represented by lavas and hypabyssal rocks, which show distinctive characteristics when  
618 compared to the pyroclastic rocks. These characteristics include porphyritic texture with a  
619 relative abundance of phenocrysts in a microcrystalline and pilotaxitic groundmass, as well  
620 as the absence of broken crystals, juvenile pyroclasts (pumice, fiamme, glass shards), and  
621 welding foliations.



622 In both effusive and explosive deposits, textural variations of the crystal populations  
623 (phenocryst, microphenocryst, and microlite) suggest changes in the composition,  
624 temperature, viscosity, and H<sub>2</sub>O content before and during the eruption. These magmatic  
625 changes produced textures such as resorption embayments, reaction rims, and  
626 devitrification features that can help us understanding the thermal evolution of the studied  
627 melts.

628 The presence of embayed and round outlines in quartz and sanidine phenocrysts in  
629 rhyolitic ignimbrites and hypabyssal dacites can be generated due to either semi-adiabatic  
630 magma ascent or magma mixing and mingling (Müller et al., 2003, 2005). In the adiabatic  
631 decompression, SiO<sub>2</sub> solubility of the phenocryst-rich magmas increases as the pressure  
632 decreases, and, as result, phenocrysts that were initially in equilibrium with the melt are  
633 partially resorbed in pre-eruptive conditions (McPhie et al., 1993). The hypothesis of  
634 magma mixing and mingling for the development of resorption embayments seems  
635 unlikely in the studied rocks, since the typical characteristics of this process, such as  
636 plagioclase-mantled K-feldspar, sieve textured plagioclase and mafic micro enclaves  
637 (Muller et al., 2005) are absent in the studied samples.

638 For the Iricoumé Group samples, the calculated T<sub>L</sub> ranging from 920 to 1110 °C  
639 provides an estimation of the magma generation temperature under anhydrous conditions.  
640 Additionally, T<sub>Zr</sub> values indicate the upper temperature limits in the magma chamber before  
641 the eruption. Viscosity calculations at T<sub>L</sub> range from 5.5 to 8.0 log Pa.s, considerably lower  
642 values when compared to the estimated viscosities at T<sub>Zr</sub>, owing to the temperature contrast  
643 between T<sub>L</sub> and T<sub>Zr</sub> (Table 3).

644 In contrast, Igarapé Paboca Formation melts present even higher T<sub>L</sub> and lower  
645 viscosities, which can be linked to the compositional differences between these two units  
646 (Table 3). Despite the strong effect of temperature on melt viscosity, the models used in

647 this study account for the non-arrhenian behavior of silicate melts, allowing a more  
648 comprehensive evaluation of the compositional effect of the studied melts on magma  
649 rheology (Giordano et al., 2006, 2008).

650 Barreto et al. (2014) based on Nd isotopic data, showed that parental magmas of the  
651 Iricoumé Group may have originated from the melting of crustal sources, likely Rhyacian.  
652 This is in agreement with Bryan et al. (2002), who suggest that the occurrence of SLIPs  
653 requires partial melting of the crust, which is favored by the presence of hydrated, high-K  
654 calc-alkaline andesites and amphibolites. As a consequence, Iricoumé samples are  
655 predominantly composed of more evolved terms, such as rhyolites and dacites, which show  
656 considerable contents of network-forming elements such as Si, O<sub>2</sub>, Ti, Al, and Fe (Barreto  
657 et al., 2014; Silva et al., 2019), in concordance with the observed high-viscosity values in  
658 this study (Fig. 10B).

659

#### 660 *5.1.1. Water effect on eruption dynamics*

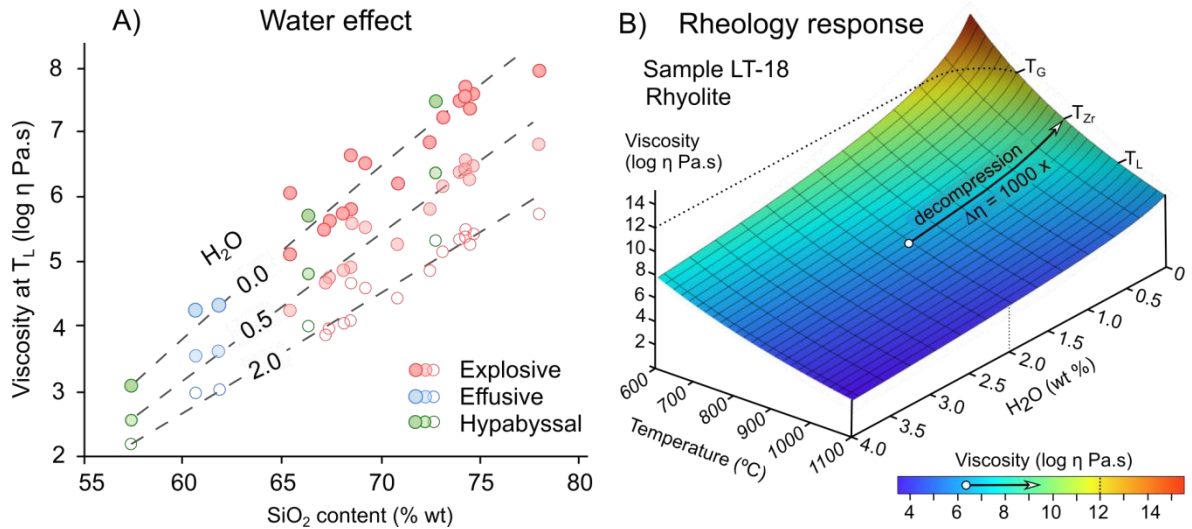
661 The high viscosities under anhydrous conditions (Fig. 11B) may suggest the presence  
662 of some viscosity-reducing agent to allow magma ascent and eruption of the studied melts.  
663 The presence of water in the studied magmas could be responsible for exponentially  
664 reducing the melt viscosity, accelerating the ascent process that leads to fragmentation by  
665 decompression.

666 Textural evidence for the presence of water in the magma consists of rimmed  
667 amphibole phenocrysts, sometimes completely replaced by oxides observed in the andesitic  
668 lavas, lamprophyres, and ignimbrites (Figs. 7A, 8A-8D). This reaction texture suggests  
669 dehydration processes during magma ascent, comprising release of vapor phase from the  
670 magma chamber and onset of explosive processes (Buckley et al., 2006; Roverato et al.,  
671 2017). The partial replacement of amphibole phenocrysts by magnetite-rich opacitic

672 texture reinforces the role of dehydration reactions during fast magma ascent (Buckley et al.  
673 2006, Cruz et al. 2014; Lagler 2019).

674 Other studies developed in the northern Amazonian Craton, in both Trombetas and  
675 Pitinga regions also identified the occurrence of amphiboles in the Iricoumé Group  
676 samples (Pierosan et al., 2011a; Silva et al., 2019). These findings seem to support a  
677 hydrous scenario for the volcanism of the Iricoumé Group, which could explain the  
678 explosive nature of this volcanism. Recent experiments by Forte and Castro (2019) have  
679 shown that H<sub>2</sub>O may dictate the eruption dynamics, inducing overpressure and  
680 fragmentation in natural samples with H<sub>2</sub>O contents as low as 1.4 wt.%, when heated  
681 above the T<sub>G</sub>.

682 In rhyolite melts, the amount of dissolved water can reach values up to 6 wt.%, that  
683 strongly affect melt viscosity and eruption dynamics (Kohn, 2000; Gonnermann and  
684 Manga, 2012; Forte and Castro, 2019). Simulations of progressive hydrous compositions  
685 (0.25, 1.0, 2.0, and 4.0 wt% H<sub>2</sub>O) of the studied samples show that even small additions of  
686 H<sub>2</sub>O (< 1 wt.%) can lead to a considerable decrease of both melt viscosity (up to 2 order of  
687 magnitude, according to the model of Giordano et al., (2008)) and temperature (T<sub>L</sub> and T<sub>G</sub>)  
688 (Table 3 and Fig. 11A). The H<sub>2</sub>O effect also seems to be stronger in more evolved magmas,  
689 where larger contrasts of viscosity and temperature among hydrous and anhydrous  
690 compositions of the same melt can be observed (Fig. 11A).



691

692

693

694

695

696

697

698

699

700

701

702

703

704

705

706

707

708

709

**Fig. 10.** Water effect on the studied melts: a) plot of H<sub>2</sub>O effect on melt viscosity; b) rheological model showing the interplay among H<sub>2</sub>O content, temperature, and viscosity. Δη = viscosity contrast during decompression.

To better understand the interplay of water content and temperature over magma rheology, we build a rheological model using a sample with an average composition of the Iricoumé Group (sample LT-18: rhyolitic ignimbrite). This model demonstrates the addition of 0.5 wt. % H<sub>2</sub>O causes a change of viscosity equivalent to a temperature increase of 100 °C (Fig. 10B; Grunder and Russell, 2005). This model also shows that, although the H<sub>2</sub>O reduces the viscosity, the loss of this dissolved hypothetical H<sub>2</sub>O due to sudden decompression may also lead to an increase up to a thousand times in melt viscosity (Δη in Fig. 11B), ultimately resulting in an explosive event.

The rheology calculations demonstrated that a considerable amount of magmatic water may be lost due to decompression and phase separation (Forte and Castro, 2019). Still, the remaining water can strongly affect the emplacement dynamics, reducing viscosity and T<sub>G</sub> (Giordano et al., 2005) resulting in porosity loss and welding (Friedman et al., 1963; Grunder and Russell, 2005).

710 *5.2. Emplacement conditions*

711 *5.2.1. Explosive products*

712 The studied ignimbrites correspond to dense pyroclastic flow regime and show typical  
713 characteristics of mass flow-dominated deposits, such as massive aspect and poor sorting,  
714 characterized by angular fragments of juvenile components, crystals and lithic clasts.  
715 Crystal fragments record the fragmentation caused by the expansion of bubbles in the  
716 magma during the eruptive decompression (Best and Christiansen, 1997).

717 Rheological data suggest a predominance of high temperatures for the samples of the  
718 Iricoumé Group ( $T_{Zr}$  ranging from 729 to 867 °C) and Igarapé Paboca Formation ( $T_{Zr}$   
719 ranging from 851 to 871 °C). These data are supported by field data with the predominance  
720 of welded, high-grade ignimbrites in the study area, which is in agreement with the other  
721 studies developed in rocks of the Iricoumé Group (Ferron et al., 2010; Pierosan et al.,  
722 2011a, 2011b; Barreto et al., 2013; Silva et al., 2019). This implies that several ignimbrites  
723 were deposited under high temperature conditions, above the calculated  $T_G$ , which allowed  
724 ductile deformation of juvenile pyroclasts (Branney and Kokelaar, 2002).

725 Additional evidence of high-temperature emplacement of the Iricoumé ignimbrites  
726 includes thermally oxidized pyroclasts, flow-foliations, and the widespread presence of  
727 eutaxitic (rank II) and parataxitic (rank III) textures. All these characteristics imply a hot,  
728 gas-supported flow emplacement in which turbulent shear-induced tractional segregation is  
729 suppressed (Branney and Kokelaar, 2002). Rapid chilling of silicate melt produces silicic  
730 glass, which may be replaced by spherulites and granophyric textures due to high-  
731 temperature devitrification and/or hydration (Logfren, 1970, 1971a, 1971b; Friedman and  
732 Long, 1984; Breikreuz, 2013). Both effusive and pyroclastic rocks of the studied area  
733 display spherulitic textures including spherical, axiolite, fan-type spherulites, as well as  
734 granophyric. The types of devitrification textures can provide a clue to the history of the

735 sub-solidus cooling under high-temperature conditions that occurred in the studied rocks  
736 (e.g., Logfren, 1971a, 1971b).

737 The first stage of devitrification consists of the development of abundant microlites  
738 and spherical spherulites (Logfren, 1971b). Swanson et al. (1989) defined that abundant  
739 small microlites represent metastable crystallization in response to a relatively high degree  
740 of undercooling. Logfren (1971a) demonstrated that spherical spherulites form at low  
741 temperatures ( $< 400^{\circ}\text{C}$ ), and their small diameters reflect a quick drop in temperature  
742 below the  $T_G$ , consistent with the rapid cooling rate. In contrast, spherulites of axiolite and  
743 fan types form at high temperatures ( $700^{\circ}\text{C}$ ) and then are followed by a second  
744 devitrification stage, which is responsible for the development of granophyric texture  
745 (Logfren, 1971a). As a result of these high-temperature processes, the ancient silicic  
746 volcanic rocks of the studied region are dominated by spherulitic or granophyric textural  
747 facies, which indicates that their groundmasses were formerly glassy, but now the glass is  
748 overprinted by devitrification and recrystallization to a quartz-feldspar mosaic due to later  
749 alteration (McPhie et al., 1993).

750 The incipiently welded ignimbrites with high crystals contents (apparent  
751 porphyritic texture with granophyric groundmass - rank I) occur in minor volume and  
752 display weak flow-foliations generated by welding. This high concentration of crystal  
753 fragments and lithic clasts (Fig. 5A, 5B, 5D, 5E) suggests the existence of elutriation  
754 processes of the glassy material of ash size in portions highly fluidized in the pyroclastic  
755 flow or even in the eruption column. This would lead to an accumulation of crystals and  
756 lithic clasts and the extraction of fine-down into secondary plumes during pyroclastic flow  
757 eruption and transport (Cas and Wright, 1987). The temperatures ( $T_{Zr}$ ) in these ignimbrites  
758 are generally just a few degrees above the minimum welding temperature, i.e., the glass  
759 transition temperature ( $T_G$ ), as observed in Fig. 10C. The large difference observed

760 between  $T_L$  and  $T_G$  suggests that welding is possible in these cases, however, the high  
761 content of crystals in these ignimbrites inhibits more pronounced welding.

762

#### 763 5.2.1.1. *Welding*

764 Historically, welding has been associated with processes of load-induced compaction  
765 and the rheological properties of the involved particles (Freundt, 1998; Branney and  
766 Kokelaar, 2002). More recently, this view has been challenged by the observation of  
767 deposits with complex welding patterns, including upward increasing in the welding  
768 degree (Soriano et al., 2002). In high-grade ignimbrites, the rheological parameters of the  
769 pyroclasts seem to play a major role, since low-viscosity particles can weld under minimal  
770 loading (Sumner and Branney, 2002).

771 The difference between emplacement and glass transition temperatures ( $\Delta T_{Zr} - T_G$ ) can  
772 be used as a proxy for welding potential, considering that the higher emplacement  
773 temperatures may result in more welded, high-grade ignimbrites. According to our  
774 rheological calculations, the studied ignimbrites show a progressive increase in welding  
775 intensity as a function of  $\Delta T_{Zr} - T_G$  (Fig. 10D). This relationship implies a direct association  
776 between eruption temperatures and welding, suggesting either a proximal source for the  
777 ignimbrite deposits and/or an eruption column able to maintain high temperatures.

778 Using field and experimental data, Roche et al. (2016) showed that welding results  
779 from the deposition of sustained, dense PDCs. More recently, Pacheco-Hoyos et al. (2017)  
780 demonstrated that welding is mainly associated with little to no mixing with ambient air  
781 during flow, allowing high deposition temperatures and favoring viscous deformation of  
782 the pyroclasts.

783 The cooling rate of the pyroclasts also affects welding, since low cooling rates result in  
784 lower  $T_G$ , granting a wider welding window (Webb, 1997; Giordano et al., 2005). Low

785 cooling rates can be achieved by fast burial and isolation, which ultimately requires high  
786 discharge rates and low mixing with ambient air. Recently, Trolese et al. (2019)  
787 demonstrate based on 3D numerical simulations that large volumes of welded ignimbrites  
788 often display low-height eruption columns. In these cases, the plume-air mixing is  
789 inefficient, resulting in high-temperature PDCs emplaced just a few degrees below  
790 eruption temperatures.

791 Welding seems to be especially prevalent in deposits of peralkaline composition,  
792 which are richer in network-modifier cations (e.g., Na<sup>+</sup>, K<sup>+</sup>, Ca<sup>2+</sup>, Mg<sup>2+</sup>), since these  
793 elements can reduce the polymerization and decreasing viscosity by several orders of  
794 magnitude, granting a higher welding window (Freundt, 1998; Grunder and Russell, 2005;  
795 Giordano et al., 2008). However, the studied samples present peraluminous to moderately  
796 metaluminous character (Barreto et al., 2014). The controversial behavior of the welded  
797 ignimbrites deposited under high temperature and viscosity conditions requires additional  
798 parameters to explain the welding foliations that are indicative of high flow-mobility. As  
799 explored in the eruption dynamics section, the presence of residual magmatic water could  
800 facilitate welding in the studied samples by considerably lowering the T<sub>G</sub> by several  
801 degrees (Table 3; Fig. 10A, 10B), as predicted by previous models and experiments  
802 (Giordano et al, 2004, 2006, 2008).

803

#### 804 *5.2.2. Effusive deposits*

805 The data obtained in this study show that the andesitic magmas of the Igarapé Paboca  
806 Formation possibly had low mobility, due to their physical characteristics which include a  
807 high percentage of phenocrysts (30-50% vol) and high content of microlites (Fig. 8), which  
808 is supported by viscosity estimations (Fig. 10). The observed high viscosities in the  
809 andesitic lava flows are comparable to values observed in lava domes (Yokoyama, 2009),



810 suggesting that the effusive episodes generated either length-limited andesitic lava flows or  
811 andesitic lava domes. As discussed above, taking into account that even a few tenths wt.%  
812 H<sub>2</sub>O can strongly influence magma rheology (Giordano et al., 2006, 2008), a more hydrous  
813 magma condition may counterbalance the effect phenocrysts in the effusive deposits,  
814 allowing the magmatic ascent and eruption as lava flows. Unfortunately, the erosion level  
815 in the study area does not allow the verification of diagnostic field features (Silva et al.,  
816 2019), such as dome morphology or the presence of margined autoclastic breccias.

817 In addition to the andesites, the effusive eruptive style also generated spessartitic  
818 lamprophyres and dacites that exhibit a hypabyssal nature. This hypabyssal emplacement is  
819 explained, in the lamprophyre case, because they normally occur as dykes (Le Maitre,  
820 2002) and, in the dacite case, because they show vertical to sub-vertical flow-foliations that  
821 can be interpreted as roots of fissural feeding systems (Fig. 4G).

822

### 823 *5.3. Reconstruction of the volcanic environment*

824 Despite the challenges related to this ancient volcanic setting, the field,  
825 petrographic and rheological data presented in this study allow us to provide a  
826 reconstruction of the volcanic environment that generated the extensive volcanic units  
827 present in this region. The results showed that there is a large volume of pyroclastic rocks  
828 with moderate- to high welding degrees in the studied area when compared with the  
829 effusive deposits.

830 It is important to note that due to the intense uplift and magmatism, only the deeper  
831 features of SLIPs may be preserved, such as caldera collapse structures, granite intrusions,  
832 and dike swarms (Bryan et al., 2002). In contrast, the tectonic stability of the Amazonian  
833 Craton from Orosirian onward, combined with arid climate conditions (Cunha, 2006) and  
834 the fast burial of the volcanoclastic units (Juliani and Fernandes, 2010) seem to have

835 contributed to the exceptional preservation of the volcanoclastic sequences (Barreto et al.,  
836 2013; Roverato et al., 2019). Therefore, this proportion could be apparent and just refer to  
837 enabling strongly welded rocks to be better preserved instead of effusive and unwelded  
838 matrix-supported pyroclastic rocks that are easily weathered, eroded, and transported in a  
839 subaerial environment.

840 The textural analysis of the studied volcanic rocks indicates that the emplacement  
841 temperatures of the two Orosirian volcanic episodes of the Erepecuru-Trombetas region are  
842 progressively higher from southwest towards northeast. The first episode is recorded by the  
843 Igarapé Paboca Formation, which represents the 1.99 Ga older volcanism in the region  
844 (Barreto et al. 2013; Castro et al., 2014; Silva et al., 2019), responsible for the  
845 emplacement of subaerial explosive rocks (incipiently welded lapilli-tuffs to moderately  
846 welded ignimbrites), in association to andesitic magmatic pulses of effusive nature.

847 The second and main volcanic episode of 1.88 Ga (Barreto et al., 2013; Castro et al.,  
848 2014; Silva et al., 2019) reveals the existence of an expressive explosive event that  
849 produced the Iricoumé Group, marked by the presence of ignimbrites. During this episode  
850 predominated pyroclastic density currents which generated incipiently welded crystal-rich  
851 ignimbrites and rhyolitic-dacitic ignimbrites with distinct welding degrees. A late volcanic  
852 episode related to the Iricoumé Group is represented by effusive spessartitic lamprophyres  
853 and dacites that occur as dykes and crosscut the volcanic stratigraphy, which is reinforced  
854 by ages ranging from 1.99 Ga to 1.88 Ga of a dacite sample (Vianna et al., 2017).

855 Geochronological, geochemical, and isotopic data show that the Iricoumé Group  
856 magmatism in the Erepecuru-Trombetas took place in a post-collisional setting (Barreto et  
857 al., 2014), and is likely associated with the development of mantle plume (Teixeira et al.,  
858 2019). This setting suggests a strong structural control on the emplacement of Iricoumé  
859 Group, in which pre-existing structures would act in two ways: 1) facilitating the

860 connection with the multiple regional magma reservoirs (Forte and Castro, 2019); 2)  
861 governing the development of calderas and fissure ignimbrite. Similar geodynamic settings  
862 have been observed in other regions of the world (e.g., Aguirre-Diaz and Labarthe-  
863 Hernandez, 2003; Spinks et al., 2005; Robertson et al., 2015).

864 Under anhydrous conditions, the studied samples of the Iricoumé Group present high  
865  $T_L$  ranging from 920 to 1110 °C, frequently > 1000 °C (Table 3). These values are  
866 comparable to  $T_L$  estimations for ‘dry’ SLIPs (Bryan et al., 2002; Simões et al., 2014b),  
867 and considerably higher when compared to other minor silicic systems in southern Brazil  
868 (Sommer et al., 2013; Santos et al., 2019; Haag et al., 2021), and around the world (e.g.,  
869 Grunder, 1977; Clemens et al., 1986; King et al., 1997; Patino-Dulce, 1997; Dall’Agnol et  
870 al., 1999; Hergt et al., 2007). In contrast, the older Igarapé Paboca magmatism seems to  
871 present even higher temperatures ( $T_L > 1100$  °C) and a predominance of less evolved terms,  
872 such as andesites and dacites (Barreto et al., 2013; Silva et al., 2019).

873 In addition to that, the estimated  $T_{Zr}$  in this study agree with previous estimations  
874 performed in Iricoumé Group rocks in the Uatumã-Anauá Domain (Fig. 1B) in the Pitinga  
875 region, where  $T_{Zr}$  estimations ranged from 799 to 984 °C (Ferron et al., 2010; Pierosan et  
876 al., 2011b; Simões et al., 2014a). These high temperatures are supported by field and  
877 petrographic data, in particular, high-temperature devitrification features and evidence of  
878 ductile deformation as a result of welding processes. The high temperature calculations  
879 obtained in this study for both effusive and explosive deposits associated with high-  
880 temperature textural features allow us to suggest a volcanic environment with high-  
881 discharge, continuous, and low eruptive column dynamics, typical of calderas and/or  
882 fissure-fed ignimbrites (Cas and Wright, 1987; Lowell, 1991; Aguirre-Diaz and Labarthe-  
883 Hernandez, 2003).

884 Polyphase evolution with alternation of both effusive and explosive pulses is a  
885 common feature in caldera-related environments (Lipman, 1984, 2000) and has been  
886 described in other domains of the Amazonian Craton (Pierosan, et al. 2011; Lagler et al.,  
887 2019) and the Paleoproterozoic Kaapvaal craton (Oberholzer and Eriksson, 2000). Due to  
888 the extensive occurrence of explosive rocks related to the Iricoumé Group (mainly welded  
889 ignimbrites) and analog units in the Amazonian Craton, a few calderas have been proposed  
890 as possible sources for these rocks (e.g., Ferron et al., 2010; Pierosan et al., 2011b; Lagler  
891 et al., 2019). Most of these putative calderas have been proposed based on geomorphologic  
892 attributes, such as relief and drainage patterns since access to most of these areas is still  
893 difficult (Pierosan et al., 2011b). However, the number of proposed calderas is still scarce  
894 when compared to the extension of more than 1.2 million km<sup>2</sup> of outcropping volcanic  
895 rocks associated with the Uatumã event (Roverato et al., 2016).

896 The apparent absence of caldera-collapse structures in the Erepecuru-Trombetas region,  
897 along with structural and field evidence, led us to an alternative hypothesis involving  
898 fissure-fed ignimbrites for the emplacement of the studied rocks in the region (*sensu*  
899 Aguirre-Diaz and Labarthe-Hernandez, 2003). This environment for the generation of the  
900 volcanic sequences has been proposed for the Tapajós and Iriri-Xingu domains, both  
901 located in the southern Amazonian Craton (e.g., Juliani and Fernandes, 2010; Roverato et  
902 al., 2019). In this model, regional faults act as conduits, yielding high-temperature and  
903 voluminous ignimbrite sequences followed by aligned rhyolitic lava domes (Aguirre-Diaz  
904 and Labarthe-Hernandez, 2003; Juliani and Fernandes, 2010).

905 Estimations of pressure and oxygen fugacity for calcic amphiboles performed by  
906 Pierosan et al. (2011a) in the Pitinga region (Uatumã-Anauá Domain; Fig. 1) indicate  
907 pressure conditions of 0.5 to 1.0 kbar and depths of ~ 2 Km, compatible with shallow  
908 magma chambers (Walker, 2008). At the time of the Uatumã magmatism emplacement,

909 lithospheric thinning and extension related to mantle plume impact in the lithosphere  
 910 would result in axial faults and the development of basin and range structures, exploiting  
 911 pre-existing collisional structures. These faults can reach depths of 20 km (Hamilton, 1987)  
 912 that could easily connect with the shallow magma chambers in the region, leading to  
 913 sudden decompression and triggering voluminous fissural and caldera ignimbrite eruptions  
 914 (Fig. 12). The presence of a strong structural control marked by NW-SE regional faults in  
 915 the Erepecuru-Trombetas domain (see Fig. 2; Silva et al., 2019) could reinforce this  
 916 hypothesis.

917

918

919

920

921

922

923

924

925

926

927

928

929

930

931

932

933

934

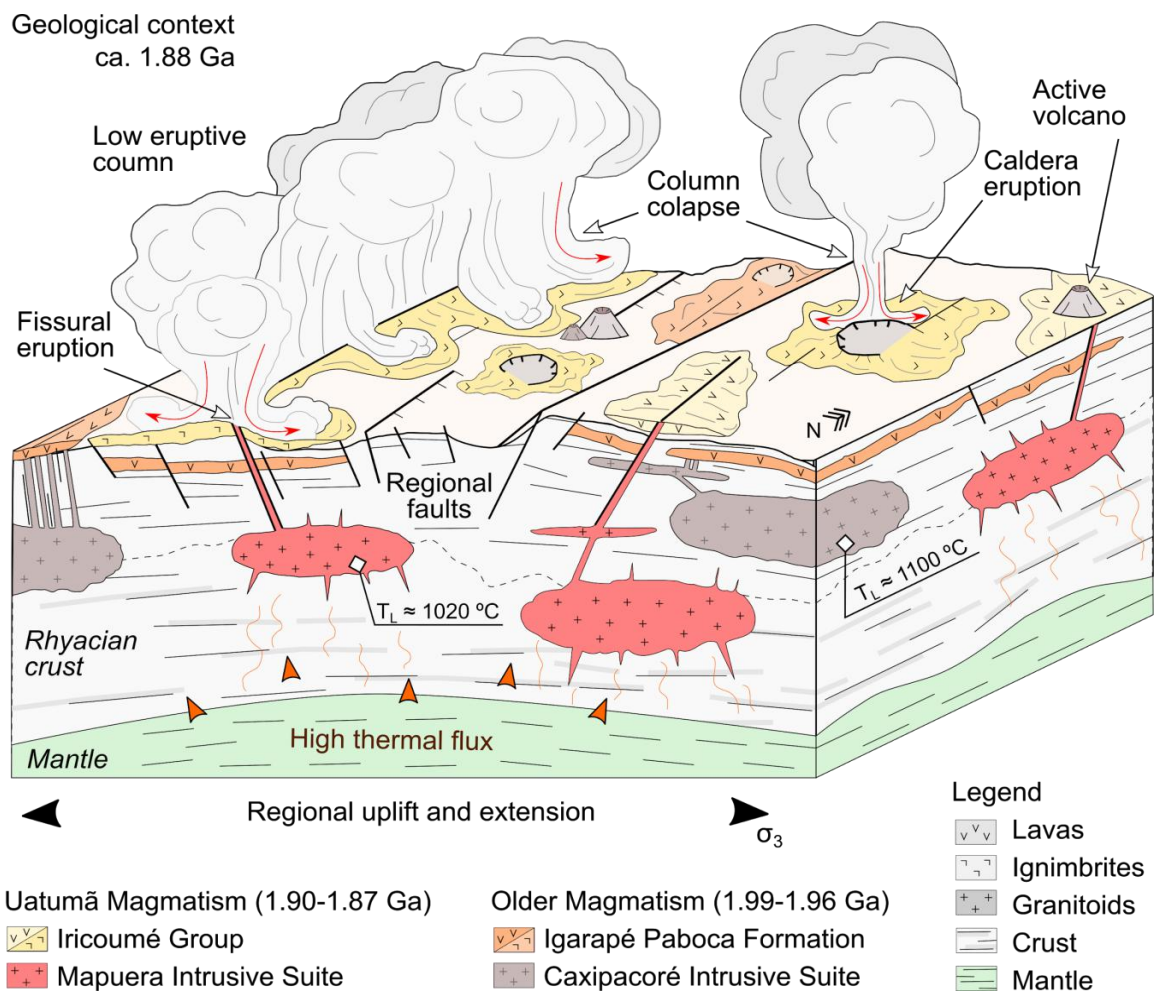


**Fig. 12.** Reconstruction of the volcanic history in the Erepecuru-Trombetas region: regional context in which regional faults exploit shallow magma chambers, triggering voluminous explosive fissure-fed and caldera eruptions.

935 **6. Concluding remarks**

936 This study indicates a large volume of pyroclastic rocks with moderate to high welding  
937 degrees in the studied area. The main results are:

938 1. Two Orosirian volcanic episodes predominate in the Erepecuru-Trombetas region:  
939 the 1.99 Ga Igarapé Paboca Formation (subaerial explosive rocks and effusive pulses of  
940 andesitic composition), and the 1.88 Ga Iricoumé Group (mainly composed of subaerial  
941 explosive rock). A late volcanic episode related to the Iricoumé Group is represented by  
942 effusive spessartitic lamprophyres and dacites that crosscut the volcanic stratigraphy.

943 2. Rheological data suggest a predominance of high temperatures for the samples of  
944 the Iricoumé Group ( $T_{Zr}$  ranging from 729 to 867 °C) and Igarapé Paboca Formation ( $T_{Zr}$   
945 ranging from 851 to 871 °C). These data are supported by the textural evidences that  
946 include thermally oxidized pyroclasts, extensive welding and rheomorphism.

947 3. Ignimbrites show a increase in welding intensity as a function of  $\Delta T_{Zr}-T_G$ . This  
948 implies a hot, gas-supported PDC emplacement and a direct association between eruption  
949 and emplacement temperatures. This suggests a volcanic environment with a high-  
950 discharge and low eruptive column dynamics and/or a proximal source, compatible with  
951 both caldera and fissure-fed ignimbrites.

952 4. Rheological data suggest that even small additions of H<sub>2</sub>O can lead to a considerable  
953 decreasing of both melt viscosity and temperature ( $T_L$  and  $T_G$ ), resulting in porosity loss  
954 and welding. This should accelerate the magma ascent and enhance fragmentation by  
955 decompression, as supported by petrographic evidence.

956 This study provides rheological boundaries and an environmental reconstruction  
957 supported by textural analysis and rheological parameter calculations. However, more  
958 detailed studies of volcanic stratigraphy with lithofacies associations are necessary to

959 define proximal to distal facies and fully reconstruct the Orosirian volcanism in the  
960 northern Amazon Craton.

961

## 962 **Acknowledgements**

963 We acknowledge the CNPq/Universal project (Grant 484571/2007-9) for financial  
964 support and CPRM/Belém for taking the samples used in this study. The authors are  
965 grateful to reviews of Joan Martí, Matteo Roverato and the editor Wilson Teixeira by  
966 provided important suggestions to improvement of the manuscript.

967

968

969

970

971

972

973

974

975

976

977

978

979

980

981

982

983

984 **References**

- 985 Aguirre-Díaz, G.J., Labarthe-Hernández, G., 2003. Fissure ignimbrites: Fissure-source  
986 origin for voluminous ignimbrites of the Sierra Madre Occidental and its relationship with  
987 Basin and Range faulting. *Geology* 31, 773. <https://doi.org/10.1130/g19665.1>
- 988 Almeida, F.F.M., Hasui, Y., de Brito Neves, B.B., Fuck, R.A., 1981. Brazilian  
989 structural provinces: An introduction. *Earth-Science Reviews* 17,1–29.  
990 [https://doi.org/10.1016/0012-8252\(81\)90003-9](https://doi.org/10.1016/0012-8252(81)90003-9)
- 991 Antonio, P.Y.J., 2016. Paleomagnetismo e petrogênese de unidades Paleoproterozóicas  
992 do evento Uatumã no norte do Cráton Amazônico. Ph.D. Thesis, University of São Paulo.  
993 Instituto de Astronomia, Geofísica e Ciências Atmosféricas, 289 p.
- 994 Antonio, P.Y.J., D'Agrella-Filho, M.S., Trindade, R.I.F., Nédélec, A., de Oliveira,  
995 D.C., da Silva, F.F., Roverato, M., Lana, C., 2017. Turmoil before the boring billion:  
996 Paleomagnetism of the 1880–1860 Ma Uatumã event in the Amazonian craton. *Gondwana*  
997 *Research* 49, 106–129. <https://doi.org/10.1016/j.gr.2017.05.006>
- 998 Barreto, C.J.S., Lafon, J.M., Rosa Costa, L.T., Lima, E.F. de, 2013. Vulcanismo  
999 félsico paleoproterozoico do Grupo Iricoumé, Domínio Erepecuru-Trombetas, Província  
1000 Amazônia Central: dados de campo, caracterização petrográfica e geocronologia Pb-Pb em  
1001 zircão. *Geologia USP. Série Científica* 13, 47–72. <https://doi.org/10.5327/z1519-874x2013000100004>
- 1002
- 1003 Barreto, C.J.S., Lafon, J.M., Rosa Costa, L.T., Lima, E.F., 2014. Palaeoproterozoic  
1004 (~1.89 Ga) felsic volcanism of the Iricoumé Group, Guyana Shield, South America:  
1005 geochemical and Sm-Nd isotopic constraints on sources and tectonic environment.  
1006 *International Geology Review* 56, 1332–1356.  
1007 <https://doi.org/10.1080/00206814.2014.930800>
- 1008 Bettencourt, J.S., Juliani, C., Xavier, R.P., Monteiro, L.V.S., Bastos Neto, A.C., Klein,  
1009 E.L., Assis, R.R., Leite, W.B., Jr., Moreto, C.P.N., Fernandes, C.M.D., Pereira, V.P., 2016.  
1010 Metallogenic systems associated with granitoid magmatism in the Amazonian Craton:  
1011 An overview of the present level of understanding and exploration significance. *Journal of*  
1012 *South American Earth Sciences* 68, 22–49. <https://doi.org/10.1016/j.jsames.2015.11.014>
- 1013 Branney, M.J., Kokelaar, P. 2002. Pyroclastic Density Currents and the Sedimentation  
1014 of Ignimbrites. Geological Society, London, Memoirs 27.
- 1015 Breitreuz, C., 2013. Spherulites and lithophysae - 200 years of investigation on high-  
1016 temperature crystallization domains in silica-rich volcanic rocks. *Bull Volcanol* 75.  
1017 <https://doi.org/10.1007/s00445-013-0705-6>
- 1018 Brito Neves, B.B., 2011. The Paleoproterozoic in the South- American continent:  
1019 Diversity in the geologic time: *Journal of South American Earth Sciences* 32, 270–286.  
1020 <https://doi.org/10.1016/j.jsames.2011.02.004>
- 1021 Bryan, S.E., Ferrari, L., 2013. Large igneous provinces and silicic large igneous  
1022 provinces: Progress in our understanding over the last 25 years. *Geological Society of*  
1023 *America Bulletin* 125, 1053–1078. <https://doi.org/10.1130/b30820.1>
- 1024 Bryan, S.E., Riley, T.R., Jerram, D.A., Stephens, C.J., Leat, P.T., 2002. Silicic  
1025 volcanism: An undervalued component of large igneous provinces and volcanic rifted  
1026 margins, in: *Volcanic Rifted Margins*. Geological Society of America.  
1027 <https://doi.org/10.1130/0-8137-2362-0.97>



- 1028 Cáceres, F., Wadsworth, F.B., Scheu, B., Colombier, M., Madonna, C., Cimarelli, C.,  
1029 Hess, K.-U., Kaliwoda, M., Ruthensteiner, B., Dingwell, D.B., 2020. Can nanolites  
1030 enhance eruption explosivity? *Geology*. <https://doi.org/10.1130/g47317.1>
- 1031 Cordani, U.G., Ramos, V.A., Fraga, L.M., Cegarra, M., Delgado, I., Souza, K.G.,  
1032 Gomes, F.E.M., Schobbenhaus, C., 2016. Tectonic map of South America, Commission  
1033 For The Geological Map of the World, Map, scale 1:5.000.000.
- 1034 Costa, A., 2005. Viscosity of high crystal content melts: Dependence on solid fraction.  
1035 *Geophysical Research Letters* 32. <https://doi.org/10.1029/2005gl024303>
- 1036 Costa, A., Caricchi, L., Bagdassarov, N., 2009. A model for the rheology of particle-  
1037 bearing suspensions and partially molten rocks. *Geochemistry, Geophysics, Geosystems* 10.  
1038 <https://doi.org/10.1029/2008gc002138>
- 1039 Di Genova, D., Kolzenburg, S., Wiesmaier, S., Dallanave, E., Neuville, D.R., Hess,  
1040 K.U., Dingwell, D.B., 2017. A compositional tipping point governing the mobilization and  
1041 eruption style of rhyolitic magma. *Nature* 552, 235–238.  
1042 <https://doi.org/10.1038/nature24488>
- 1043 Ernst, R.E., Buchan, K.L., 2001. Large mafic magmatic events through time and links  
1044 to mantle-plume heads, in: *Mantle Plumes: Their Identification through Time*. Geological  
1045 Society of America. <https://doi.org/10.1130/0-8137-2352-3.483>
- 1046 Fernandes, C.M.D., Juliani, C., Monteiro, L.V.S., Lagler, B., Echeverri Misas, C.M.,  
1047 2011. High-K calc-alkaline to A-type fissure-controlled volcano-plutonism of the São Félix  
1048 do Xingu region, Amazonian craton, Brazil: Exclusively crustal sources or only mixed Nd  
1049 model ages? *Journal of South American Earth Sciences* 32, 351–368.  
1050 <https://doi.org/10.1016/j.jsames.2011.03.004>
- 1051 Fernandes, C.M.D., Lamarão, C.N., Teixeira, N.P., 2006. O vulcanismo bimodal do  
1052 tipo Uatumã da região de São Félix do Xingu (PA). *Província Mineral de Carajás. Revista*  
1053 *Brasileira de Geociências* 36, 565–576 (in Portuguese).
- 1054 Ferron, J.M.T.M., Bastos Neto, A.C., Lima, E.F., Costi, H.T., Moura, C.A.V., Prado,  
1055 M., Pierosan, R., Galarza, M.A., 2006. Geologia e geocronologia Pb–Pb de rochas  
1056 graníticas e vulcânicas ácidas a intermediárias Paleoproterozóicas da Província Pitinga,  
1057 Craton Amazônico. *Revista Brasileira de Geociências* 36, 501–519 (in Portuguese).
- 1058 Ferron, J.M.T.M., Bastos Neto, A.C., Lima, E.F., Nardi, L.V.S., Costi, H.T., Pierosan,  
1059 R., Prado, M., 2010. Petrology, geochemistry, and geochronology of Paleoproterozoic  
1060 volcanic and granitic rocks (1.89–1.88Ga) of the Pitinga Province, Amazonian Craton,  
1061 Brazil. *Journal of South American Earth Sciences* 29, 483–497.  
1062 <https://doi.org/10.1016/j.jsames.2009.05.001>
- 1063 Forte, P., Castro, J.M., 2019. H<sub>2</sub>O-content and temperature limit the explosive  
1064 potential of rhyolite magma during Plinian eruptions. *Earth and Planetary Science Letters*  
1065 506, 157–167. <https://doi.org/10.1016/j.epsl.2018.10.041>
- 1066 Fraga, L.M.B., Cordani, U.G., 2019. Early Orosirian tectonic evolution of the Central  
1067 Guiana Shield: insights from new U-Pb SHRIMP data. In: *11th Inter Guiana Geological*  
1068 *Conference: Tectonics and Metallogensis of NE South America*. Paramaribo, Suriname,  
1069 Geologisch Mijnbouwkundige Dienst Suriname. Mededeling 29, 59-62.
- 1070 Giordano, D., Nichols, A.R.L., Dingwell, D.B., 2005. Glass transition temperatures of  
1071 natural hydrous melts: a relationship with shear viscosity and implications for the welding

- 1072 process. *Journal of Volcanology and Geothermal Research* 142, 105–118.  
1073 <https://doi.org/10.1016/j.jvolgeores.2004.10.015>
- 1074 Giordano, D., Russell, J.K., Dingwell, D.B., 2008. Viscosity of magmatic liquids: A  
1075 model. *Earth and Planetary Science Letters* 271(1–4), 123–134.  
1076 <https://doi.org/10.1016/j.epsl.2008.03.038>
- 1077 Gonnermann, H.M., Manga, M., Fagents, S.A., 2013. Dynamics of magma ascent in  
1078 the volcanic conduit, in: Gregg, T.K.P., Lopes, R.M.C. (Eds.), *Modeling Volcanic*  
1079 *Processes*. Cambridge University Press, pp. 55–84.  
1080 <https://doi.org/10.1017/cbo9781139021562.004>
- 1081 Haag, M.B., de Freitas, R.B., Sommer, C.A., Savian, J.F., Lima, E.F., Gambeta, J.H.,  
1082 Lyra, D. da S., Trindade, R.I.F. da, 2021. Multi-proxy case study of a Neoproterozoic  
1083 rhyolite flow in southernmost Brazil: Emplacement mechanisms and implications for  
1084 ancient felsic lavas. *Journal of South American Earth Sciences* 107, 102982.  
1085 <https://doi.org/10.1016/j.jsames.2020.102982>
- 1086 Hamilton, W., 1987. Crustal extension in the Basin and Range Province, southwestern  
1087 United States. *Geological Society, London, Special Publications* 28, 155–176.  
1088 <https://doi.org/10.1144/gsl.sp.1987.028.01.12>
- 1089 Juliani, C., Fernandes, C.M.D., 2010. Well-preserved Late Paleoproterozoic volcanic  
1090 centers in the São Félix do Xingu region, Amazonian Craton, Brazil. *Journal of*  
1091 *Volcanology and Geothermal Research* 191, 167–179.  
1092 <https://doi.org/10.1016/j.jvolgeores.2010.01.016>
- 1093 Juliani, C., Fernandes, C.M.D., Monteiro, L.V.S., Lagler, B., Misas, C.M.E., 2011.  
1094 Very low-grade metamorphism and very well preserved epithermal mineralization in the  
1095 Paleoproterozoic Uatumã LIP, Southern Amazonian craton, Brazil: European Geosciences  
1096 Union General Assembly, Abstracts, p. 11815.
- 1097 Klein, E.L., Almeida, M.E., Costa, L.T.R., 2012. The 1.89- 1.87 Ga Uatumã Silicic  
1098 Large Igneous Province, northern South America: Large Igneous Provinces Commission:  
1099 <http://www.largeigneousprovinces.org/12nov> (accessed 10 July 2020).
- 1100 Kohn, S.C., 2000. The dissolution mechanisms of water in silicate melts; a synthesis of  
1101 recent data. *Mineralogical Magazine* 64, 389–408.  
1102 <https://doi.org/10.1180/002646100549463>
- 1103 Lagler, B., Juliani, C., Dias Fernandes, C.M., Souza da Cruz, R., Strauss Vieira, D.A.,  
1104 2019. Paleoproterozoic volcanic caldera in the Amazonian craton, northern Brazil:  
1105 Stratigraphy, lithofacies characterization, and lithochemical constraints. *Journal of*  
1106 *South American Earth Sciences* 95, 102252. <https://doi.org/10.1016/j.jsames.2019.102252>
- 1107 Lamarão, C.N., Dall’Agnol, R., Lafon, J.-M., Lima, E.F., 2002. Geology,  
1108 geochemistry, and Pb–Pb zircon geochronology of the Paleoproterozoic magmatism of  
1109 Vila Riozinho, Tapajós Gold Province, Amazonian craton, Brazil. *Precambrian Research*  
1110 119, 189–223. [https://doi.org/10.1016/s0301-9268\(02\)00123-7](https://doi.org/10.1016/s0301-9268(02)00123-7)
- 1111 Liu, H.-Q., Xu, Y.-G., He, B., 2013. Implications from zircon-saturation temperatures  
1112 and lithological assemblages for Early Permian thermal anomaly in northwest China.  
1113 *Lithos* 182–183, 125–133. <https://doi.org/10.1016/j.lithos.2013.09.015>
- 1114 Magalhães, L.B., Lafon, J.M., Rosa-Costa, L.T., Barreto, C.J.S., Dantas, E.L., 2017.  
1115 *Geocronologia de zircões detríticos por LA-ICP-MS de cobertura sedimentar*

- 1116 Paleoproterozoica do Dominio Erepecuru-Trombetas Oeste, Província Amazônia Central.  
1117 In: Anais do 15º Simpósio de Geologia da Amazônia, Belém. p. 447-450.
- 1118 Manville, V., Németh, K., Kano, K., 2009. Source to sink: A review of three decades  
1119 of progress in the understanding of volcanoclastic processes, deposits, and hazards.  
1120 *Sedimentary Geology* 220, 136–161. <https://doi.org/10.1016/j.sedgeo.2009.04.022>
- 1121 Motta, J.G., Souza Filho, C.R. de, Carranza, E.J.M., Braitenberg, C., 2019. Archean  
1122 crust and metallogenic zones in the Amazonian Craton sensed by satellite gravity data.  
1123 *Scientific Reports* 9. <https://doi.org/10.1038/s41598-019-39171-9>
- 1124 Muller, A., Breiter, K., Seltmann, R., Pécskay, Z. 2005. Quartz and feldspar zoning in  
1125 the eastern Erzgebirge volcano-plutonic complex (Germany, Czech Republic): evidence of  
1126 multiple magma mixing. *Lithos* 80, 201-227. <https://doi.org/10.1016/j.lithos.2004.05.011>
- 1127 Muller, A., René, M., Behr, H.J., Kronz, A. 2003. Trace elements and  
1128 cathodoluminescence of igneous quartz in topaz granites from the Hub Stock (Slavkovský  
1129 Les Mts., Czech Republic). *Mineralogy and Petrology* 79, 167-191.  
1130 <https://doi.org/10.1007/s00710-003-0238-3>
- 1131 Pacheco-Hoyos, J.G., Aguirre-Díaz, G.J., Dávila-Harris, P., 2017. Boiling-over dense  
1132 pyroclastic density currents during the formation of the ~ 100 km<sup>3</sup> Huichapan ignimbrite  
1133 in Central Mexico: Stratigraphic and lithofacies analysis. *Journal of Volcanology and  
1134 Geothermal Research* 349, 268–282. <https://doi.org/10.1016/j.jvolgeores.2017.11.007>
- 1135 Pierosan, R., de Lima, E.F., Nardi, L.V.S., Bastos Neto, A.C., de Campos, C.P., Jarvis,  
1136 K., Ferron, J.M.T.M., Prado, M., 2011a. Geochemistry of Palaeoproterozoic volcanic rocks  
1137 of the Iricoumé Group, Pitinga Mining District, Amazonian craton, Brazil. *International  
1138 Geology Review* 53, 946–979. <https://doi.org/10.1080/00206810903391542>
- 1139 Pierosan, R., Lima, E.F., Nardi, L.V.S., Campos, C.P., Bastos Neto, A.C., Ferron,  
1140 J.M.T.M., Prado, M., 2011b. Paleoproterozoic (~1.88Ga) felsic volcanism of the Iricoumé  
1141 Group in the Pitinga Mining District area, Amazonian Craton, Brazil: insights in ancient  
1142 volcanic processes from field and petrologic data. *Anais da Academia Brasileira de  
1143 Ciências* 83 (3), 921–937. <http://dx.doi.org/10.1590/S0001-37652011000300012>
- 1144 Pinho, S.C.C., Fernandes, C.M.D., Teixeira, N.P., Paiva Jr., A.L., Cruz, V.L., Lamarão,  
1145 C.N., Moura, C.A.V., 2006. O magmatismo paleoproterozóico da região de São Félix do  
1146 Xingu, Província Estanífera do Sul do Pará: Petrografia e Geocronologia. *Revista  
1147 Brasileira de Geociências* 36, 793–802 (in Portuguese).
- 1148 Quane, S.L., Russell, J.K., 2004. Ranking welding intensity in pyroclastic deposits.  
1149 *Bulletin of Volcanology* 67, 129–143. <https://doi.org/10.1007/s00445-004-0367-5>
- 1150 Reis, N.J., Almeida, M.E., Riker, S.R.L., Ferreira, A.L., 2006. Geologia e Recursos  
1151 minerais do Estado do Amazonas, Manaus: CPRM, (Convênio CPRM/CIAMA). 125 p., il.  
1152 Escala 1:1.000.000.
- 1153 Reis, N.J., Fraga, L.M., Faria, M.S.G., and Almeida, M.E., 2003. Geologia do Estado  
1154 de Roraima, Brasil: Geology of France and Surrounding Areas- Special Guiana Shield, v.  
1155 2-3-4, p. 121–134.
- 1156 Robertson, E.A.M., Biggs, J., Cashman, K.V., Floyd, M.A., Vye-Brown, C., 2015.  
1157 Influence of regional tectonics and pre-existing structures on the formation of elliptical  
1158 calderas in the Kenyan Rift. *Geological Society, London, Special Publications* 420, 43–67.  
1159 <https://doi.org/10.1144/sp420.12>

- 1160 Roverato, M., 2016. The Montesbelos mass-flow (southern Amazonian craton, Brazil):  
1161 a Paleoproterozoic volcanic debris avalanche deposit? *Bull Volcanol* 78.  
1162 <https://doi.org/10.1007/s00445-016-1043-2>
- 1163 Roverato, M., Giordano, D., Echeverri-Misas, C.M., Juliani, C., 2016.  
1164 Paleoproterozoic felsic volcanism of the Tapajós Mineral Province, Southern Amazon  
1165 Craton, Brazil. *Journal of Volcanology and Geothermal Research* 310, 98–106.  
1166 <https://doi.org/10.1016/j.jvolgeores.2015.11.019>
- 1167 Roverato, M., Juliani, C., Dias-Fernandes, C.M., Capra, L., 2017. Paleoproterozoic  
1168 andesitic volcanism in the southern Amazonian craton, the Sobreiro Formation: New  
1169 insights from lithofacies analysis of the volcanoclastic sequences. *Precambrian Research*  
1170 289, 18–30. <https://doi.org/10.1016/j.precamres.2016.11.005>
- 1171 Roverato, M., Giordano, D., Giovanardi, T., Juliani, C., Polo, L., 2019. The 2.0–  
1172 1.88 Ga Paleoproterozoic evolution of the southern Amazonian Craton (Brazil): An  
1173 interpretation inferred by lithofaciological, geochemical and geochronological data.  
1174 *Gondwana Research* 70, 1–24. <https://doi.org/10.1016/j.gr.2018.12.005>
- 1175 Santos, J.O.S., Groves, D.I., Hartmann, L.A., Moura, M.A., McNaughton, N.J., 2001.  
1176 Gold deposits of the Tapajós and Alta Floresta Domains, Tapajós–Parima orogenic belt,  
1177 Amazon Craton, Brazil. *Mineralium Deposita* 36, 278–299.  
1178 <https://doi.org/10.1007/s001260100172>
- 1179 Santos, J.O.S., Hartmann, L.A., Faria, M.S., Riker, S.R., Souza, M.M., Almeida, M.E.,  
1180 McNaughton, N.J., 2006. A compartimentação do cráton amazonas em províncias: avanços  
1181 ocorridos no período 2000–2006, in *Simpósio de Geologia da Amazônia*, 9th, Atas.
- 1182 Santos, J.O.S., Hartmann, L.A., Gaudette, H.E., Groves, D.I., Mcnaughton, N.J.,  
1183 Fletcher, I.R., 2000. A New Understanding of the Provinces of the Amazon Craton Based  
1184 on Integration of Field Mapping and U-Pb and Sm-Nd Geochronology. *Gondwana*  
1185 *Research* 3, 453–488. [https://doi.org/10.1016/s1342-937x\(05\)70755-3](https://doi.org/10.1016/s1342-937x(05)70755-3)
- 1186 Santos, E.A. dos, Sommer, C.A., Waichel, B.L., Haag, M.B., 2019. Ediacaran post-  
1187 collisional high-silica volcanism associated to the Florianópolis Batholith, Dom Feliciano  
1188 Belt, southernmost Brazil: lithofacies analysis and petrology. *Journal of South American*  
1189 *Earth Sciences* 96, 102299. <https://doi.org/10.1016/j.jsames.2019.102299>
- 1190 Schindelin, J., Arganda-Carreras, I., Frise, E., Kaynig, V., Longair, M., Pietzsch, T.,  
1191 Preibisch, S., Rueden, C., Saalfeld, S., Schmid, B., Tinevez, J.-Y., White, D.J., Hartenstein,  
1192 V., Eliceiri, K., Tomancak, P., Cardona, A., 2012. Fiji: an open-source platform for  
1193 biological-image analysis. *Nature Methods* 9, 676–682.  
1194 <https://doi.org/10.1038/nmeth.2019>
- 1195 Schobbenhaus, C., Brito Neves, B.B., 2003. A Geologia do Brasil no Contexto da  
1196 Plataforma Sul-Americana, in Bizzi, L.A., Schobbenhaus, C., Vidotti, R.M., and  
1197 Gonçalves, J.H., eds., *Geologia, tectônica e Recursos Minerais do Brasil*: Brasília, CPRM,  
1198 p. 5–53.
- 1199 Silva, R.C.S., Castro, J.M.R., Rosa-Costa, L.T., Chaves, C.L., 2019. Geologia e  
1200 recursos minerais da folha Rio Trombetas SA.21-X-A, estado do Pará: texto-explicativo,  
1201 CPRM, Map, Scale 1:250.000. Available at:  
1202 <http://rigeo.cprm.gov.br/jspui/handle/doc/21492>
- 1203 Simões, M.S., Almeida, M.E., de Souza, A.G.H., da Silva, D.P.B., Rocha, P.G., 2014a.  
1204 Characterization of the volcanic and hypabissal rocks of the Paleoproterozoic Iricoumé

- 1205 Group in the Pitinga region and Balbina Lake area, Amazonian Craton, Brazil:  
1206 Petrographic distinguishing features and emplacement conditions. *Journal of Volcanology*  
1207 and *Geothermal Research* 286, 138–147. <https://doi.org/10.1016/j.jvolgeores.2014.08.024>
- 1208 Simões, M.S., Rossetti, L. de M.M., Lima, E.F. de, Ribeiro, B.P., 2014b. The role of  
1209 viscosity in the emplacement of high-temperature acidic flows of Serra Geral Formation in  
1210 Torres Syncline (Rio Grande do Sul State, Brazil). *Brazilian Journal of Geology* 44, 669–  
1211 679. <https://doi.org/10.5327/z23174889201400040010>
- 1212 Sisson, T.W., Grove, T.L., 1993. Temperatures and H<sub>2</sub>O contents of low-MgO high-  
1213 alumina basalts. *Contributions to Mineralogy and Petrology* 113(2), 167–184.  
1214 <https://doi.org/10.1007/bf00283226>
- 1215 Soriano, C., Zafrilla, S., Martí, J., Bryan, S., Cas, R., Ablay, G., 2002. Welding and  
1216 rheomorphism of phonolitic fallout deposits from the Las Cañadas caldera, Tenerife,  
1217 Canary Islands. *Geological Society of America Bulletin* 114, 883–895.  
1218 [https://doi.org/10.1130/0016-7606\(2002\)114<0883:waropf>2.0.co;2](https://doi.org/10.1130/0016-7606(2002)114<0883:waropf>2.0.co;2)
- 1219 Spinks, K.D., Acocella, V., Cole, J.W., Bassett, K.N., 2005. Structural control of  
1220 volcanism and caldera development in the transtensional Taupo Volcanic Zone, New  
1221 Zealand. *Journal of Volcanology and Geothermal Research* 144, 7–22.  
1222 <https://doi.org/10.1016/j.jvolgeores.2004.11.014>
- 1223 Tassinari, C.C.G., Macambira, M.J.B., 2004, A evolução tectônica do Cráton  
1224 Amazônico, in Mantesso Neto, V., Bartorelli, A., Dal Ré Carneiro, C., and de Brito Neves,  
1225 B.B., eds., *Geologia do continente Sul-Americano: evolução da obra de Fernando Flávio*  
1226 *Marques de Almeida: São Paulo, Beca, p. 471–485.*
- 1227 Teixeira, W., Nelson, J.R., Bettencourt, J.S., Klein, E.L., Oliveira, D.C., 2019.  
1228 Intraplate Proterozoic magmatism in the Amazonian Craton reviewed: geochronology,  
1229 crustal tectonics and global matches. *Dyke Swarms of the World: A Modern Perspective*  
1230 [https://doi.org/10.1007/978-981-13-1666-1\\_4](https://doi.org/10.1007/978-981-13-1666-1_4)
- 1231 Vasquez, M.L., Costa, L.T.R., 2008, *Mapa Geológico e de Recursos Minerais do*  
1232 *Estado do Pará. Projeto Geologia e Recursos Minerais do Pará – Sistema de Informações*  
1233 *Geográficas: texto-explicativo, Belém, CPRM, Mapa, col. Escala 1:1.000.000. 1 CD-ROM.*
- 1234 Vernon, R.H. 2004. *A practical guide to Rock Microstructure.* Cambridge University  
1235 Press, New York, p. 655.
- 1236 Vianna, S.Q., Magalhães, L.B., Lafon, J.M., Rosa-Costa, L.T. 2017. Geocronologia U-  
1237 Pb e Pb-Pb e geoquímica isotópica Sr-Nd da porção oeste do Domínio Erepecuru -  
1238 Trombetas, Província Amazônia Central, noroeste do Pará. In: *Anais do 15º Simpósio de*  
1239 *Geologia da Amazônia, Belém. p. 451-454.*
- 1240 Walter, T.R., 2008. Chapter 9 Facilitating Dike Intrusions into Ring-Faults, in: *Caldera*  
1241 *Volcanism: Analysis, Modelling and Response.* Elsevier, pp. 351–374.  
1242 [https://doi.org/10.1016/s1871-644x\(07\)00009-5](https://doi.org/10.1016/s1871-644x(07)00009-5)
- 1243 Watson, E.B., 1979. Zircon saturation in felsic liquids: Experimental results and  
1244 applications to trace element geochemistry. *Contributions to Mineralogy and Petrology* 70,  
1245 407–419. <https://doi.org/10.1007/bf00371047>
- 1246 Watson, E.B., Harrison, T.M., 1983. Zircon saturation revisited: temperature and  
1247 composition effects in a variety of crustal magma types. *Earth and Planetary Science*  
1248 *Letters* 64, 295–304. [https://doi.org/10.1016/0012-821x\(83\)90211-x](https://doi.org/10.1016/0012-821x(83)90211-x)

- 1249 Webb, S., 1997. Silicate melts: Relaxation, rheology, and the glass transition. *Reviews*  
1250 *of Geophysics* 35, 191–218. <https://doi.org/10.1029/96rg03263>
- 1251 Yokoyama, I., 2009. Growth rates of lava domes with respect to viscosity of magmas.  
1252 *Annals of Geophysics* 48. <https://doi.org/10.4401/ag-3246>